Computational Mechanics (2024) 73:297–316
https://doi.org/10.1007/s00466-023-02368-x

ORIGINAL PAPER

Updated Lagrangian particle hydrodynamics (ULPH) modeling for free-surface fluid flows

Jiale Yan[1,2,3] · Shaofan Li[4] · Xingyu Kan[5] · Pengyu Lv[1,2] · A-Man Zhang[3] · Huiling Duan[1,2]

Received: 27 February 2023 / Accepted: 5 July 2023 / Published online: 8 September 2023

Abstract
In this work, we develop an accurate and stable Updated Lagrangian particle hydrodynamics (ULPH) modeling to simulate complicated free-surface fluid flows. Leveraging its inherent properties as a Lagrangian particle method, the ULPH has natural advantages in modeling free-surface flows. However, similar to other meshfree methods, ULPH is subject to numerical instabilities and non-physical pressure fluctuations when solving the Navier–Stokes equation in the explicit numerical scheme. Within the framework of the ULPH method, several innovative enhanced treatment techniques have been proposed and combined with other previouly developed methods to establish an ULPH single-phase flow model. The main novelties of these techniques are the derivation of the density diffusive term in the continuum equation inspired by δ-SPH to eliminate pressure oscillations, and the proposal of a new free-surface search algorithm to determine the particles and their normal vectors at the free surface. The ULPH is a nonlocal fluid dynamics model, which is in fact a prototype of Peridynamics in fluid mechanics. Considering the nature of free-surface fluid flows, we strategically implement the diagonalization and renormalization of the shape tensor for particles located in close proximity to the free-surface region to improve the numerical stability of computations. Several complex free-surface flow benchmark examples have been simulated, which confirms that the enhanced treatment techniques can effectively capture the details of surface flow evolution and maintain long-term stability. Moreover, the qualitative and quantitative analyses of the results indicate that the proposed ULPH surface flow model is highly accurate and stable for simulating complex free-surface fluid flows.

Keywords Computational fluid dynamics · Density diffusive term · Free-surface flows · Free-surface detection · Peridynamics · Updated Lagrangian particle hydrodynamics (ULPH)

1 Introduction

Free-surface fluid flows are a common occurrence in both natural phenomena and industrial applications, especially in hydraulic and ocean engineering, as well as environmental fluid mechanics engineering and sciences. Manifestations of such phenomena encompass a diverse range of events such as flood flow, dam breaks, tsunami waves, offshore waves and tidal bore, ship waves, liquid sloshing, water entry, deck waves, among others. These events are often associated with or dictated by intense nonlinear physical phenomena, including large deformations of free surfaces, rolling and breaking of waves, and splashing of liquid droplets. These free-surface flows can induce violent impact loads on hydraulic, offshore, and naval or marine structures. Evaluating these impact loads is very important for designing engineering structures to guarantee the human safety as well as the safety of civil operations, facilities, and equipment.

✉ Huiling Duan
hlduan@pku.edu.cn

1 State Key Laboratory for Turbulence and Complex Systems, Department of Mechanics and Engineering Science, BIC-ESAT, College of Engineering, Peking University, Beijing 100871, China

2 Joint Laboratory of Marine Hydrodynamics and Ocean Engineering, Laoshan Laboratory, Qingdao 266237, China

3 College of Shipbuilding Engineering, Harbin Engineering University, Harbin 150001, China

4 Department of Civil and Environmental Engineering, University of California, Berkeley, CA 94720, USA

5 Key Laboratory for Mechanics in Fluid Solid Coupling Systems, Institute of Mechanics, Chinese Academy of Sciences, Beijing 100190, China

Over the years, the fluid dynamics of free-surface flows has been extensively investigated in numerical modelings by many researchers. However, the development of robust and efficient numerical techniques for accurately simulating complex free-surface fluid flows continues to present a significant challenge. For grid-based methods, such as Finite Volume Method (FVM) [1], Finite Difference Method (FDM) [2] and Finite Element Method (FEM) [3], the evolution of physical quantities is carried out on grid nodes, which are significantly influenced by the connectivity of the grid. The flexibility of FVM and FEM lies in their adaptability to unstructured grids, allowing them to effectively handle complex geometries. To simulate free-surface flows, specifically in situations involving substantial interface deformation, supplementary techniques such as volume of fluid (VOF) [4, 5] and level set (LS) [6, 7] methods are often necessary in these grid-based approaches. However, it's worth acknowledging that the implementation of these additional techniques to track and capture changing free surfaces can require significant computational resources. Conversely, meshfree methods, which are intrinsically Lagrangian, possess inherent advantages in addressing complex free-surface flows. Typical particle methods of this kind include Smoothed Particle Hydrodynamics (SPH) [8–10], Material Point Method (MPM) [11, 12], Moving Particle Semi-implicit method (MPS) [13, 14], and Reproducing kernel particle method (RKPM) [15], etc.

SPH is a well-known particle method initially proposed for modeling astrophysical problems [16] before being adapted for simulating free-surface flows by Monaghan [17]. Through continuous improvement and development, SPH has been widely employed to simulate violent free-surface flows, such as sloshing flows [18], wave breaking [19], bubble dynamics [20], tsunami flows [21], hydroelastic impact [22], etc. The MPS method, which was proposed by Koshizuka and Oak [13], has demonstrated success in simulating complex hydrodynamic environments [23–25]. The MPM method was proposed by Sulsky et al. [26], which has the advantages of Eulerian and Lagrangian methods and can deal with free-surface flow problems with large deformations [27, 28].

Recently, Tu and Li [29] proposed a novel meshfree particle method to solve hydrodynamics problems, namely Updated Lagrangian Particle Hydrodynamics (ULPH), which is inspired by Peridynamics [30, 31] and SPH [32], and it is essentially a prototype of nonlocal computational fluid dynamics model. As a Lagrangian meshfree particle method, the ULPH is based on nonlocal theory and nonlocal differential operators. In ULPH, the nonlocal differential operators are utilized to decouple the fluid governing equations discretely. Since the accuracy of nonlocal differential operator depends on the polynomial basis, it can achieve any order of precision that one desires [33–36]. Therefore, ULPH has a higher accuracy compared to that of the conventional SPH. Yan et al. [33, 37] have developed the ULPH multiphase flow model for simulating complex multiphase flows with high viscosity and density ratios. Liu et al. [38] have coupled ULPH with PD to investigate the motion and damage characteristics of ice when it was impacted by a sphere under ice-water interaction. Despite these advancements, to date, there has been no application of the ULPH model specifically to free-surface fluid flows. The development of a unified ULPH single-phase flow model may hold the potential to significantly enhance the current state of free-surface fluid flow simulation technology.

The primary objective of this work is to develop an accurate and stable ULPH single-phase flow model for simulating complex free-surface flows. To accomplish that, we will first establish the ULPH basic scheme for free-surface flows based on nonlocal theory. Thanks to the Lagrangian meshfree feature, ULPH can easily simulate violent free-surface flows with large deformations by directly tracking particles. Despite the strong capacities of ULPH, it also suffers from numerical instabilities and non-physical pressure fluctuations like other meshfree methods, which are mainly caused by errors due to Lagrange motion and the weakly compressible hypothesis. The Lagrangian particles follow the streamlines, and, to some extent, they will lead to non-uniform particle distributions and particle clustering. To ensure numerical stabilities and eliminate pressure fluctuations, several innovative enhanced treatment techniques have been proposed within the framework of ULPH modeling. A conservative density diffusive term is added into the continuity equation to handle spurious numerical fluctuations in the density/pressure fields. This term is derived from Taylor series expansion, motivated by the δ-SPH method [39–41]. The particle shifting technology [42] is also adopted in the ULPH single-phase flow model to correct particle positions and prevent particle clustering. Based on the properties of the dimensionless moment matrix and the geometric features of the free surface, a new method for identifying free-surface particles is proposed. In addition, an optimal moment matrix is developed for particles near free surface, which can effectively eliminate the ill-conditioned moment matrix and significantly improve the numerical stability. By using these enhanced treatment techniques, the proposed ULPH single-phase flow model can be well applied to various complex free-surface fluid flows.

The rest of this paper is organized as follows. Section 2 presents the governing equations and ULPH scheme for free-surface flows. Subsequently, some processing techniques to enhance numerical stability and accuracy, such as the density diffusive term, particle shifting technology, free-surface detection approach and optimal moment matrix at the free-surface vicinity, are also introduced in this section. In Sect. 3, by using the proposed method, some challenging and well-known free-surface flow benchmark cases are simulated to

validate the accuracy and significance of the proposed ULPH single-phase flow model. Finally, we conclude the work in Sect. 4, providing remarks and future perspectives on the proposed method.

2 ULPH free-surface fluid flow model

In this section, we outline the principal methodology of the Updated Lagrangian Particle Hydrodynamics (ULPH) method and present the proposed technical ingredients for the ULPH free-surface flow model.

2.1 Governing equations

For general weakly compressible barotropic fluids, the governing equations in the Lagrangian form [43] are expressed as

$$\begin{cases} \frac{\mathrm{D}\rho}{\mathrm{D}t} = -\rho\nabla\cdot\mathbf{v} \\ \rho\frac{\mathrm{D}\mathbf{v}}{\mathrm{D}t} = -\nabla\mathrm{p} + \mathbf{F}_v + \rho\mathbf{g} \\ \frac{\mathrm{D}\mathbf{r}}{\mathrm{D}t} = \mathbf{v} \end{cases} \tag{1}$$

where ρ, $\mathbf{v}$ and p respectively represent the fluid density, velocity and pressure, $\mathbf{F}_v$ is the viscous force, $\mathbf{g}$ is gravitational acceleration, and $\mathbf{r}$ indicates the position of fluid particles.

In system (1), it is closed by the equation of state (EOS) to construct the relationship between the fluid density and pressure. Following the assumption of weakly compressible fluid, a linear equation of state [44] is adopted as

$$\mathrm{p} = c_0^2\,(\rho - \rho_0) \tag{2}$$

where c_0 and ρ_0 represent the reference speed of sound and reference density, respectively. The EOS limits the density variation to less than 1%, which is in accordance with the assumption of a weakly compressible fluid, as the Mach number of the fluid is kept below 0.1. Since the simulation time step selection is straightly connected to the conditions for stability, the artificial sound speed of $c_0 \geq 10\mathrm{V}_{\max}$ is chosen as the reference value rather than the actual physical sound speed to get a reasonable time step, with $\mathrm{V}_{\max}$ being the maximum expected velocity.

2.2 ULPH scheme for free-surface fluid flows

In the ULPH method, nonlocal differential operators derived from Taylor series expansion are adopted to calculate common differential operators [33], such as divergence, gradient and curl. The feature of the nonlocal differential operator is that its support holds a finite characteristic length, and it can be regarded as a generalization of the local operator. When the support of the nonlocal differential operator degenerates to a single point, the nonlocal differential operator will reduce to the local operator. The nonlocal divergence operator and nonlocal gradient operator [33] are respectively defined as follows:

$$\nabla_I\cdot(\bullet) := \int_{\mathscr{H}_I} \omega(\boldsymbol{x}_{IJ})\big(\triangle(\bullet)\big)\cdot\big(\mathbf{M}_I^{-1}\boldsymbol{x}_{IJ}\big)\mathrm{d}V_J \tag{3}$$

$$\nabla_I\otimes(\bullet) := \int_{\mathscr{H}_I} \omega(\boldsymbol{x}_{IJ})\big(\triangle(\bullet)\big)\otimes\big(\mathbf{M}_I^{-1}\boldsymbol{x}_{IJ}\big)\mathrm{d}V_J \tag{4}$$

where symbol $(\bullet)$ represents the arbitrary field, and $\triangle(\bullet) := (\bullet)_J - (\bullet)_I$ is the finite difference operator. $\mathscr{H}_I$ indicates the support domain of particle I, referred to as the horizon, the subscript J represents the J-th particle within the horizon of particle I, and $\boldsymbol{x}_{IJ} = \boldsymbol{x}_J - \boldsymbol{x}_I$. $\omega(\boldsymbol{x}_{IJ})$ is the kernel function and must meet specific criteria, such as symmetry, normalization and compactness. The influence domain of the kernel function is determined by the smoothing length, denoted by h. In this study, the Wendland kernel function [45] is employed with $h = 2\Delta x$, where Δx indicates the initial particle spacing. $\mathbf{M}$ represents the moment matrix with symmetric properties defined as

$$\mathbf{M}_I := \int_{\mathscr{H}_I} \omega(\boldsymbol{x}_{IJ})\boldsymbol{x}_{IJ}\otimes\boldsymbol{x}_{IJ}\mathrm{d}V_J. \tag{5}$$

As a Lagrangian particle method, the ULPH method requires the discretization of the computational domain into particles with physical properties. Therefore, nonlocal differential operators presented in Eqs. (3) and (4) can be expressed in the particle approximation form [33] as follows:

$$\nabla_I\cdot(\bullet) = \sum_{J=1}^{N} \omega(\boldsymbol{x}_{IJ})\big(\triangle(\bullet)\big)\cdot\big(\mathbf{M}_I^{-1}\boldsymbol{x}_{IJ}\big)V_J \tag{6}$$

$$\nabla_I\otimes(\bullet) = \sum_{J=1}^{N} \omega(\boldsymbol{x}_{IJ})\big(\triangle(\bullet)\big)\otimes\big(\mathbf{M}_I^{-1}\boldsymbol{x}_{IJ}\big)V_J \tag{7}$$

in which N represents the neighboring particle number of particle I.

The moment matrix defined in Eq. (5) is discretized in the particle approximation form as

$$\mathbf{M}_I = \sum_{J=1}^{N} \omega(\boldsymbol{x}_{IJ})\boldsymbol{x}_{IJ}\otimes\boldsymbol{x}_{IJ}V_J. \tag{8}$$

Based on the above nonlocal differential operators and Peridynamic theory [30], governing equations of the ULPH model [43] are defined as follows:

$$\begin{cases} \frac{\mathrm{D}\rho_I}{\mathrm{D}t} = -\rho_I \sum_{J=1}^{N} \omega\left(\boldsymbol{x}_{IJ}\right)\left(\mathbf{v}_J - \mathbf{v}_I\right)\mathbf{M}_I^{-1}\boldsymbol{x}_{IJ}V_J, \\ \frac{\mathrm{D}\mathbf{v}_I}{\mathrm{D}t} = -\frac{1}{\rho_I}\sum_{J=1}^{N}\omega\left(\boldsymbol{x}_{IJ}\right)\left(\mathrm{p}_J\mathbf{M}_J^{-1} + \mathrm{p}_I\mathbf{M}_I^{-1}\right)\boldsymbol{x}_{IJ}V_J \\ \qquad + \frac{1}{\rho_I}\mathbf{F}_{v,I} + \mathbf{g}_I, \\ \frac{\mathrm{D}\mathbf{r}_I}{\mathrm{D}t} = \mathbf{v}_I,\ \mathrm{p}_I = c_0^2\left(\rho_I - \rho_0\right),\ V_I = \frac{m_I}{\rho_I}, \end{cases} \tag{9}$$

where the viscous force $\mathbf{F}_{v,I}$ can be approximated by an artificial viscous term Π_I in the present work, defined as

$$\Pi_I = \alpha h c_0 \rho_0 \sum_{J=1}^{N} \omega\left(\boldsymbol{x}_{IJ}\right)\pi_{IJ}\mathbf{M}_I^{-1}\boldsymbol{x}_{IJ}V_J \tag{10}$$

where α indicates the coefficient for the artificial viscous term. The term π_{IJ} in the artificial viscous term can be expressed as

$$\pi_{IJ} = \frac{\mathbf{v}_{IJ}\cdot\boldsymbol{x}_{IJ}}{|\boldsymbol{x}_{IJ}|^2 + (0.1h)^2}\,. \tag{11}$$

The relationship between parameter α and kinematic viscosity ν [46] is defined as

$$\alpha = \frac{2(n+2)}{hc_0}\nu \tag{12}$$

where n represents the spatial dimension of the problem. Consequently, the real viscosity of the fluid can be considered in the simulation by the transformation of Eq. (12). For the scope of the current work, unless explicitly state otherwise, a value of 0.1 is assigned to the parameter α when the actual viscosity of the fluid is not specifically discussed.

2.3 The density diffusive term

Since the liquid is regarded as the weakly compressible fluid in the current ULPH model, the solution procedure is completely explicit. Pressure is explicitly calculated according to the EOS, which is different from the incompressible approach implicitly calculating the pressure from the Poisson equation. Hence, the weakly compressible approach may bring out abundant unphysical pressure oscillations [43], which also has the same issue in the SPH method. Over the years of SPH development, several numerical correction methods have been proposed to address this drawback, such as density filter [39], adding conservative diffusive terms to the equation of continuity, and Riemann solvers [47], etc.

Inspired by the δ-SPH [40], introducing a density diffusive term within the continuity equation can help eliminate spurious high-frequency numerical oscillations in the density/pressure fields. Equivalent to adding an artificial viscous term to the momentum equation, the density diffusive term in the equation of continuity approximates the Laplacian of the density, $\delta\nabla^2\rho$, where $\delta = \mathscr{O}(h)$. The conservative diffusive term, which is incorporated into the continuity equation, is derived from Taylor series expansion to meet the global conservation of mass. For a generic scalar function $f(\boldsymbol{x}) \in C^2(\mathbb{R}^3)$, it holds the following Taylor series:

$$f\left(\boldsymbol{x}_J\right) = f\left(\boldsymbol{x}_I\right) + \nabla f|_I \cdot \boldsymbol{x}_{IJ} + \frac{1}{2}\boldsymbol{x}_{IJ}^T \cdot Hf|_I \cdot \boldsymbol{x}_{IJ} + \mathscr{O}(h^3) \tag{13}$$

$$f\left(\boldsymbol{x}_I\right) = f\left(\boldsymbol{x}_J\right) + \nabla f|_J \cdot \boldsymbol{x}_{JI} + \frac{1}{2}\boldsymbol{x}_{JI}^T \cdot Hf|_J \cdot \boldsymbol{x}_{JI} + \mathscr{O}(h^3) \tag{14}$$

Subtracting Eq. (13) from Eq. (14), we can get

$$2\left(f\left(\boldsymbol{x}_J\right) - f\left(\boldsymbol{x}_I\right)\right) = \left(\nabla f|_J + \nabla f|_I\right)\cdot\boldsymbol{x}_{IJ} + \boldsymbol{x}_{IJ}^T \cdot\left(\frac{Hf|_I - Hf|_J}{2}\right)\cdot\boldsymbol{x}_{IJ}. \tag{15}$$

Through further transformation, one may obtain

$$\left(\frac{Hf|_I - Hf|_J}{2}\right)\cdot\boldsymbol{x}_{IJ} = 2\frac{f\left(\boldsymbol{x}_J\right) - f\left(\boldsymbol{x}_I\right)}{\boldsymbol{x}_{IJ}} - \left(\nabla f|_J + \nabla f|_I\right). \tag{16}$$

To simplify the notation, $\left(\frac{Hf|_I - Hf|_J}{2}\right) = D(\boldsymbol{x}_I)$ is defined as conservative diffusive term:

$$D(\boldsymbol{x}_I)\cdot\boldsymbol{x}_{IJ} = 2\frac{f\left(\boldsymbol{x}_J\right) - f\left(\boldsymbol{x}_I\right)}{\boldsymbol{x}_{IJ}} - \left(\nabla f|_J + \nabla f|_I\right). \tag{17}$$

Multiplying both sides of Eq. (17) with $\omega(\boldsymbol{x}_{IJ})$ and $\boldsymbol{x}_{IJ}$, integrating over the horizon of particle I can yield the following equation

$$\begin{aligned} &\int_{\mathscr{H}_I} D\left(\boldsymbol{x}_I\right)\cdot\omega\left(\boldsymbol{x}_{IJ}\right)\boldsymbol{x}_{IJ}\otimes\boldsymbol{x}_{IJ}dV_J \\ &= \int_{\mathscr{H}_I} 2\left(f\left(\boldsymbol{x}_J\right) - f\left(\boldsymbol{x}_I\right)\right)\omega\left(\boldsymbol{x}_{IJ}\right)dV_J \\ &- \int_{\mathscr{H}_I}\left(\nabla f|_J + \nabla f|_I\right)\omega\left(\boldsymbol{x}_{IJ}\right)\boldsymbol{x}_{IJ}dV_J. \end{aligned} \tag{18}$$

Substituting Eq. (5) into Eq. (18),

$$\begin{aligned} D\left(\boldsymbol{x}_I\right)\mathbf{M}_I &= \int_{\mathscr{H}_I} 2\left(f\left(\boldsymbol{x}_J\right) - f\left(\boldsymbol{x}_I\right)\right)\omega\left(\boldsymbol{x}_{IJ}\right)dV_J \\ &- \int_{\mathscr{H}_I}\left(\nabla f|_J + \nabla f|_I\right)\omega\left(\boldsymbol{x}_{IJ}\right)\boldsymbol{x}_{IJ}dV_J. \end{aligned} \tag{19}$$

Multiplying both sides of Eq. (19) with $\mathbf{M}_I^{-1}$, Eq. (19) can be rewritten as

$$D(\boldsymbol{x}_I) = \int_{\mathscr{H}_I} 2\big(f(\boldsymbol{x}_J) - f(\boldsymbol{x}_I)\big)\omega(\boldsymbol{x}_{IJ})\,\mathbf{M}_I^{-1} dV_J - \int_{\mathscr{H}_I} \big(\nabla f|_J + \nabla f|_I\big)\,\omega(\boldsymbol{x}_{IJ})\,\mathbf{M}_I^{-1}\boldsymbol{x}_{IJ} dV_J \tag{20}$$

$$D(\boldsymbol{x}_I) = \int_{\mathscr{H}_I} \omega(\boldsymbol{x}_{IJ})\,\phi_{IJ}\mathbf{M}_I^{-1}\boldsymbol{x}_{IJ} dV_J \tag{21}$$

where the term ϕ_{IJ} is defined as

$$\phi_{IJ} = \frac{2\left(f(\boldsymbol{x}_J) - f(\boldsymbol{x}_I)\right)\boldsymbol{x}_{IJ}}{|\boldsymbol{x}_{IJ}|^2} - \big(\nabla f|_J + \nabla f|_I\big). \tag{22}$$

Subsequently, Eq. (21) can be expressed in the discrete form as

$$D(\boldsymbol{x}_I) = \sum_{J=1}^{N} \omega(\boldsymbol{x}_{IJ})\,\phi_{IJ}\mathbf{M}_I^{-1}\boldsymbol{x}_{IJ} V_J. \tag{23}$$

Similar to the form of artificial viscous term, the coefficient δ, smoothing length h and initial sound speed c_0 should be multiplied by Eq. (23) to control the magnitude of the density diffusive term

$$\Phi_I = \delta h c_0 \sum_{J=1}^{N} \omega(\boldsymbol{x}_{IJ})\,\phi_{IJ}\mathbf{M}_I^{-1}\boldsymbol{x}_{IJ} V_J. \tag{24}$$

For all numerical simulations, the coefficient δ is set to 0.1, unless otherwise stated. Finally, the continuity equation with the density diffusive term can be rewritten as

$$\frac{D\rho_I}{Dt} = -\rho_I \sum_{J=1}^{N} \omega(\boldsymbol{x}_{IJ})\,(\mathbf{v}_J - \mathbf{v}_I)\,\mathbf{M}_I^{-1}\boldsymbol{x}_{IJ} V_J + \Phi_I. \tag{25}$$

2.4 Particle shifting technology (PST)

For meshfree particle methods, the particles move along the streamline and corresponding Lagrangian trajectory due to solving the Navier–Stokes equation in Lagrangian form. Consequently, particle stretching and compressing occur under specific conditions, which may lead to particle aggregation and tensile instability. These inherent weaknesses of meshfree methods will influence the numerical stability and accuracy. To eliminate these drawbacks and enhance the numerical stability, the particle shifting technology (PST) is widely applied in meshfree particle methods for simulating fluid flows. Xu et al. [42] initially implemented the PST in the incompressible SPH method to correct particle positions, where the particle shifting vector is calculated by neighboring particles. The distribution of particles is nearly uniform after shifting, which will reduce the singularity of the particle distribution.

In the present work, we adopt the PST developed by Xu et al. [42] in the ULPH model. The particle position is corrected by a shifting vector as

$$\boldsymbol{x}_{I'} = \boldsymbol{x}_I + \delta\boldsymbol{x}_I \tag{26}$$

where $\boldsymbol{x}_I$ represents the position of particle I before shifting, while $\boldsymbol{x}_{I'}$ denotes the position after shifting. The shifting vector δx_I is expressed as

$$\delta\boldsymbol{x}_I = C\zeta\mathbf{R}_I \tag{27}$$

where C is the coefficient ranging from 0.01 to 0.1. A value of 0.04 is generally adopted. ζ is the shifting magnitude defined as

$$\zeta = \mathrm{V}_{\max}\Delta t \tag{28}$$

where $\mathrm{V}_{\max}$ and Δt respectively represent the maximum expected velocity and time step.

The shifting direction $\mathbf{R}_I$ is defined as

$$\mathbf{R}_I = \sum_{J=1}^{N} \frac{|\bar{x}_I|^2}{|\boldsymbol{x}_{IJ}|^2}\boldsymbol{\xi}_{IJ} \tag{29}$$

where $|\boldsymbol{x}_{IJ}|$ represents the distance between particle I and particle J, $|\bar{x}_I|$ denotes the average particle distance within the particle I horizon, defined as

$$\bar{x}_I = \frac{1}{N}\sum_{J=1}^{N} |\boldsymbol{x}_{IJ}|. \tag{30}$$

$\boldsymbol{\xi}$ denotes the unit distance vector between particle I and particle J, expressed as

$$\boldsymbol{\xi}_{IJ} = \frac{\boldsymbol{x}_{IJ}}{|\boldsymbol{x}_{IJ}|}. \tag{31}$$

The summation of $\boldsymbol{\xi}_{IJ}$ represents the anisotropy of particle spacings, and $|\bar{x}_I|^2/|\boldsymbol{x}_{IJ}|^2$ performs as a weighting function to decrease the influence of remote neighbouring particles. It is worth noting that the distances of particle shifting are significant enough to avoid particle clustering, but they are still considerably shorter than convection distances. Exceeding the convection distances with particle shifting can introduce other numerical errors during simulation. Due to fluid particles moving along streamlines, the maximum particle shifting distance should be less than $0.2\Delta x$.

As an optional step, the velocity field can be updated based on a Taylor series approximation after the particles have been shifted, which can be defined as follows:

$$\mathbf{v}_{I'} = \mathbf{v}_I + \delta \boldsymbol{x}_I \cdot \nabla \mathbf{v}_I \ . \tag{32}$$

Considering that the pressure field is not utilized in predicting the subsequent time step, the pressure field is not updated after the particle shifting. Since the calculated particle shifting distance is relatively small compared to the particle spacing within a time step, the updated velocity is only slightly different from the previous velocity. Consequently, the linear correction of Eq. (32) can also be disregarded after implementing the PST in the present work.

2.5 Free-surface detection method

On account of the kernel truncation, when the PST is employed to free-surface flow simulations, Eq. (27) may calculate the inaccurate shifting vector $\delta \boldsymbol{x}_I$ for the particles near or belonging to the free surface [48]. Therefore, some special treatments are necessary for free-surface particles and their neighbor particles when applying PST. Identifying the free-surface particles located on the free-surface region is a crucial step, and it involves a two-stage detection algorithm:

(1) Detecting particles in the free-surface vicinity region based on the properties of dimensionless moment matrix;
(2) Detecting particles that are actually part of the free surface by examining their geometric properties and evaluating their normals.

In the first step, it calculates the minimum eigenvalue of the dimensionless moment matrix defined as

$$\mathbf{M}_I^D = \sum_{J=1}^{N} \omega\left(\boldsymbol{x}_{IJ}\right) \frac{\boldsymbol{x}_{IJ}}{\Delta x} \otimes \frac{\boldsymbol{x}_{IJ}}{\Delta x} V_J \tag{33}$$

where Δx is the initial particle distance. The value of the minimum eigenvalue λ of the dimensionless moment matrix $\mathbf{M}_I^D$ is influenced by the spatial distribution of the particles J within the horizon of particle I. The smoothing length h also affects the minimum eigenvalue λ. Different smoothing lengths adopted in the weighting function will have distinct minimum eigenvalues of $\mathbf{M}_I^D$, because the smoothing length influences the particle number in the domain. For a specific smoothing length h, the change range of minimum eigenvalues in the computational domain will be fixed. According to the characteristic of the smallest eigenvalue λ of the dimensionless shape tensor, the particles in the free-surface vicinity region can be identified.

In the present work, using the ULPH method to simulate free-surface fluid flows, the Wendland kernel function [45] with the smoothing length $h = 2\Delta x$ is adopted. As a result, it must be considered that all the results and conclusions drawn in the present work are only valid for $h/\Delta x = 2$, as mentioned above.

Several tests have been conducted to determine appropriate thresholds for the eigenvalue λ. By calculating the minimum eigenvalues, free-surface particles can be roughly identified. As particles approach the free surface, the minimum eigenvalue λ tends to be 0, while for internal particles λ tends to be 1.1. The particles with $\lambda < 0.6$ are identified as free-surface particles ($I \in \mathbb{F}$), while the particles with $\lambda > 1$ are classified as internal particles ($I \in \mathbb{I}$). When the eigenvalues of particles lie between 0.6 and 1, an additional step is required to differentiate free-surface particles from internal particles.

In the second step, an umbrella-shaped region [49], defined by local normal vector to the free surface, is employed to detect free-surface particles, as illustrated in Fig. 1, which is based on the geometrical rules. This umbrella-shaped region contains two subregions, namely R_1 and R_2, respectively. In the two-dimensional case, the criterion that determines whether the candidate particle J resides within the umbrella-shaped region of particle I [49] is defined as

$$\begin{cases} \forall J \in |\boldsymbol{x}_{IJ}| \geq \sqrt{2}h \text{ and } |\boldsymbol{x}_{SJ}| < h, & J \in R_1 \\ \forall J \in |\boldsymbol{x}_{IJ}| < \sqrt{2}h \text{ and} & \\ \quad (|\boldsymbol{n}_I \cdot \boldsymbol{x}_{SJ}| + |\boldsymbol{\tau}_I \cdot \boldsymbol{x}_{SJ}|) < h, & J \in R_2 \end{cases} \tag{34}$$

where S represents the point that is situated at a distance of h from particle I, in a direction perpendicular to the free surface. $\boldsymbol{n}$ and $\boldsymbol{\tau}$ respectively denote the local unit normal vector and tangential vector of the free surface.

In the three-dimensional case, the criterion [49] is defined as

$$\begin{cases} \forall J \in |\boldsymbol{x}_{IJ}| \geq \sqrt{2}h \text{ and } |\boldsymbol{x}_{SJ}| < h, & J \in R_1 \\ \forall J \in |\boldsymbol{x}_{IJ}| < \sqrt{2}h \text{ and} & \\ \quad \arccos\left(\frac{|\boldsymbol{n}_I \cdot \boldsymbol{x}_{IJ}|}{|\boldsymbol{x}_{IJ}|}\right) < \frac{\pi}{4}, & J \in R_2 \end{cases} \tag{35}$$

If there are no neighbor particles in the region of R_1 and R_2, the concerned particles are identified as free-surface particles ($I \in \mathbb{F}$).

As illustrated in Fig. 1, the fluid particles containing free-surface particles within their horizon are specified as free-surface vicinity particles ($I \in \mathbb{F}_v$). When there are no other particles in the fluid particle horizon, this particle is regarded as a splashed particle ($I \in \mathbb{S}$). The local unit normal vector $\boldsymbol{n}$ of particle I in the free-surface region can be calculated by the spatial gradient of λ as

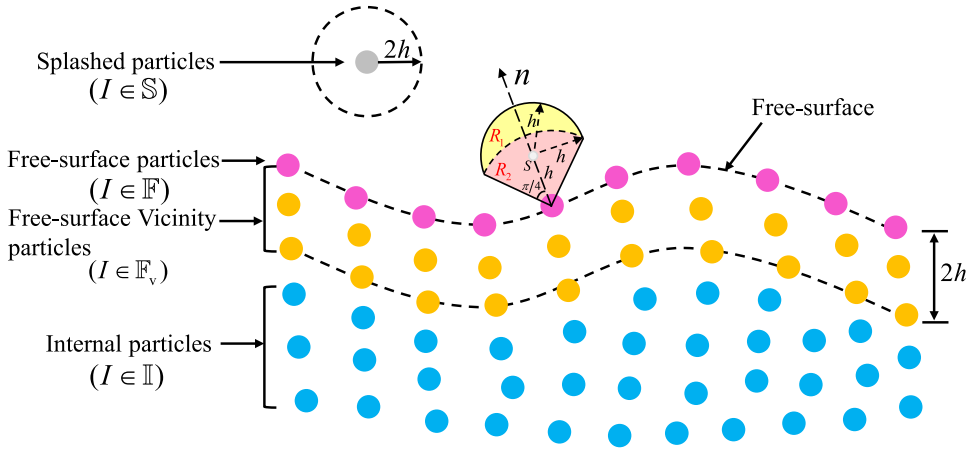

Fig. 1 Schematic illustration of free-surface vicinity particles and the defined umbrella-shaped region at the free surface

$$\boldsymbol{n}_I = \frac{\nabla \lambda_I}{|\nabla \lambda_I|} \tag{36}$$

where $\nabla \lambda_I$ is solved by the nonlocal gradient operator as

$$\nabla \lambda_I = \sum_{J=1}^{N} \omega(\boldsymbol{x}_{IJ})(\lambda_J - \lambda_I) \otimes (\mathbf{M}_I^{-1} \boldsymbol{x}_{IJ}) V_J. \tag{37}$$

Another condition that should be considered is that when the fluid flow is violent, the free surface may form thin jets. Due to the small number of neighbor particles, the normal vectors calculated at these thin jet regions may be less accurate, which will cause spurious numerical influences in the PST. Therefore, the PST should be switched off in these regions which are identified by $\lambda < 0.4$. Other particles in the vicinity of a free surface are exclusively displaced in the tangential direction of the free surface without any displacement occurring in the normal direction.

Finally, the particle in diverse regions will be shifted with different values, defined as

$$\delta \hat{\boldsymbol{x}}_I = \begin{cases} 0 & \text{if} \quad \lambda_I < 0.4 \text{ and } I \in \mathbb{F}_v \cup \mathbb{S} \\ (\mathbf{I} - \boldsymbol{n}_I \otimes \boldsymbol{n}_I)\, \delta \boldsymbol{x}_I & \text{if} \quad \lambda_I \geq 0.4 \text{ and } I \in \mathbb{F}_v \\ \delta \boldsymbol{x}_I & \text{if} \quad I \in \mathbb{I} \end{cases} \tag{38}$$

where $\mathbf{I}$ is the identity tensor.

To evaluate the exactness of the proposed algorithm for detecting free surface, a classical two-dimensional dam break simulation is conducted. The initial setup of the dam break is presented in Fig. 2. The water column has a length and height of 0.6 m and 0.3 m, respectively, where is located in a rectangular tank with the size of [1.6 m × 1.0 m]. The density of water is $\rho = 1000\,\mathrm{kg/m^3}$, and it is subjected to the acceleration of gravity $g = 9.81\,\mathrm{m/s^2}$. The initial particle distance in the computational domain is set as $\Delta x = 0.01$ m, and the dimensionless time is defined as $T = t\sqrt{g/h}$.

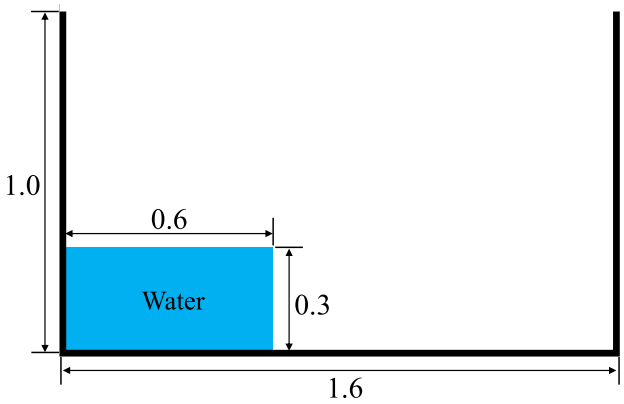

Fig. 2 The initial configuration of the two-dimensional dam break problem

Figure 3 shows the outcomes of the free-surface detection method and the normal direction at the free-surface region at $T = 2.06$ and $T = 5.72$. In the figure, the green particles represent the fluid particles located at the free surface, the red particles indicate the inner particles within the vicinity of the free surface, and the blue particles illustrate the internal fluid. The figure demonstrates that the free-surface search approach proposed in this paper can effectively identify the particles at the free surface, and accurately calculate the normal of fluid particles near the free-surface region. Consequently, it can be concluded that the free-surface search algorithm proposed in this paper has good accuracy and robustness.

2.6 Optimal moment matrix at the free-surface vicinity

In the nonlocal differential operators, the moment matrix has an essential influence on the calculation accuracy. As the matrix inversion is required in the nonlocal differential operators, the moment matrix will be ill-conditioned when the particle distribution is highly disordered and neighbor par-

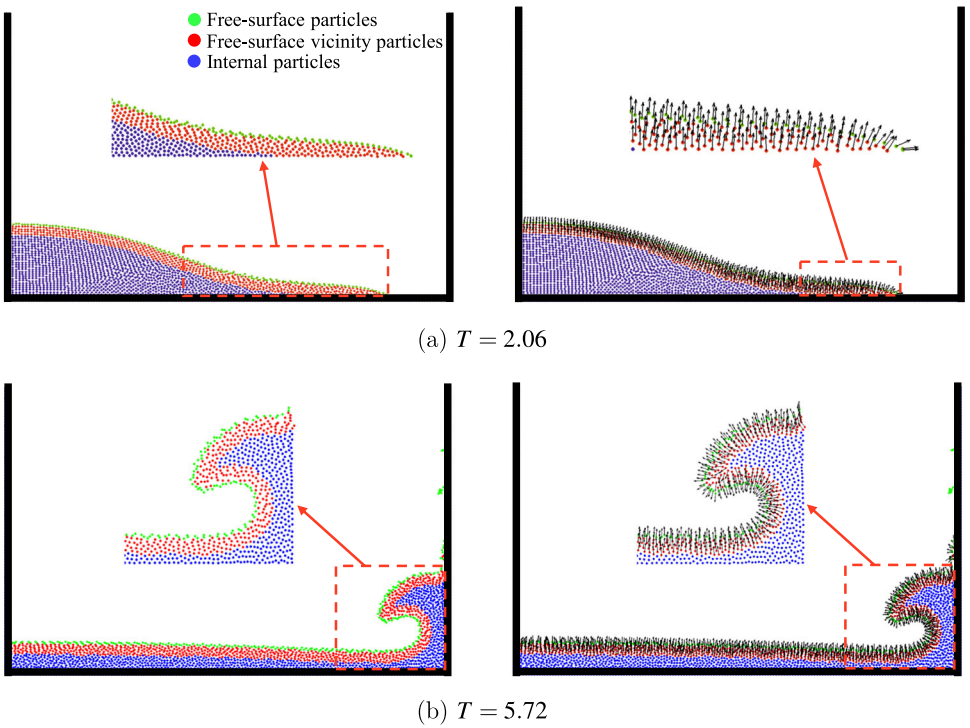

(a) $T = 2.06$

(b) $T = 5.72$

Fig. 3 The free surface search results (left column) and the normal vector at the free-surface region (right column) of the two-dimensional dam break at different times

ticles in the horizon are largely missing [43]. It will cause numerical instability and may even terminate the simulation.

For the violent free-surface flows, the moment matrix may be ill-conditioned at the free-surface vicinity. To maintain the numerical stability, we have developed an optimal moment matrix for particles located in the free-surface vicinity. When calculating the derivative of a specific direction, it is reasonable to assume that the contribution of this direction is dominant, while the contribution of other directions is insignificant and can be neglected. The elements on the off-diagonal of the moment matrix are close to zero, when the particles are in the uniform distribution and the matrix has full rank. This characteristic is similar to the evaluation of partial derivatives in the finite difference method, where the partial derivatives in a specific direction are usually replaced by finite differences in the same direction. Based on this assumption, the moment matrix for particles in the free-surface vicinity in three-dimensional space can be optimized into the following form by ignoring contributions from other directions:

$$\mathbf{M}'_I = \begin{pmatrix} \sum_{J=1}^{N} \omega(\boldsymbol{x}_{IJ})(x_J - x_I)^2 V_J & 0 & 0 \\ 0 & \sum_{J=1}^{N} \omega(\boldsymbol{x}_{IJ})(y_J - y_I)^2 V_J & 0 \\ 0 & 0 & \sum_{J=1}^{N} \omega(\boldsymbol{x}_{IJ})(z_J - z_I)^2 V_J \end{pmatrix}. \tag{39}$$

It can be seen that the optimal moment matrix $\mathbf{M}'_I$ is a diagonal matrix with zero off-diagonal elements. Therefore, the inverse of the optimal moment matrix is obtained by replacing each element in the diagonal with its reciprocal, which improves the calculation efficiency. The optimal moment matrix can not only avoid the ill-condition of the original moment matrix, but also keep the accuracy of the simulation.

As a consequence, the moment matrix $\mathbf{M}$ of particles at the free-surface vicinity identified by the free-surface detection algorithm proposed in Sect. 2.5 should be replaced by the optimal moment matrix $\mathbf{M}'$ to participate in the solution of governing equations.

2.7 Time integration

Considering the ULPH is an explicit time integration method, the predictor–corrector method [43] is used for time integration, and the time step size should satisfy the following Courant–Friedrichs–Levy (CFL) condition

$$\Delta t \leq 0.25\min\left\{\frac{h}{c+\mathrm{V}_{\max}};\sqrt{\frac{h}{|\mathbf{a}_{\max}|}}\right\} \tag{40}$$

where $\mathrm{V}_{\max}$ represents the expected maximum velocity and $\mathbf{a}_{\max}$ indicates the acceleration of fluid particles.

3 Numerical examples

This section presents several numerical cases of free-surface flows to reveal the accuracy and effectiveness of the ULPH modeling and simulation. Furthermore, the comparisons are made between the ULPH results and the experimental results as well as other numerical solutions.

3.1 Oscillating droplet under a central conservative force field

Firstly, a classic two-dimensional water droplet benchmark, situated within a central conservative force field, is conducted to investigate the performance of the proposed ULPH single-phase flow model. This test case serves as a well-established benchmark for validating numerical schemes, primarily due to its theoretical solution initially proposed by Monaghan and Rafiee [50]. The body force acting upon the fluid is a conservative force field of per unit mass [51, 52], defined as

$$\begin{cases} f_x = -\Psi^2 x \\ f_y = -\Psi^2 y \end{cases} \tag{41}$$

where Ψ is a dimensional parameter and is assigned a value of 1.2. The fluid density is $\rho_0 = 1000\ \mathrm{kg/m^3}$, and it is considered to be non-viscous and incompressible. The initial droplet is circular, possessing a radius of $R = 0.5$ m. The velocity field of the droplet at the initial state is defined as

$$\begin{cases} u_0(x,y) = \Omega_0 x \\ v_0(x,y) = -\Omega_0 y \\ p_0(x,y) = \frac{\rho\Omega_0^2}{2}\left[R^2 - \left(x^2+y^2\right)\right] \end{cases} \tag{42}$$

where Ω_0 is the initial value of the transient velocity parameter and set to 0.4. The circular droplet periodically oscillates like an ellipse over time, and the period of the oscillation is $T = \sqrt{2}\pi/\Psi = 3.7$ s. The schematic of this case is shown in Fig. 4, where a and b respectively represent the semi-major and semi-minor axes of the oscillating droplet.

The theoretical solution of the single-phase oscillating droplet can be obtained according to the formulation proposed by Monaghan and Rafiee [50] in the multiphase flow

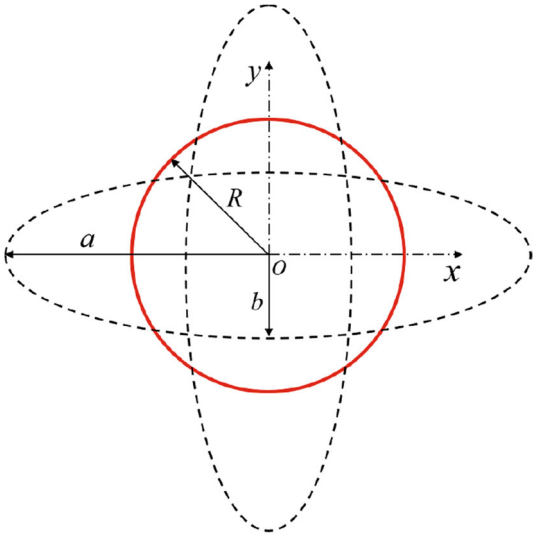

Fig. 4 Schematic diagrams of the oscillating droplet

as follows:

$$\begin{cases} \frac{d\Omega(t)}{dt} = \left(\Omega(t)^2 + \Psi^2\right)\left(\frac{b(t)^2 - a(t)^2}{a(t)^2 + b(t)^2}\right) \\ \frac{da(t)}{dt} = \Omega(t)a(t) \\ a(t)b(t) = R^2 \\ a(0) = b(0) = R \\ \Omega(0) = \Omega_0 = 0.4 \end{cases} \tag{43}$$

To assess the accuracy and convergence of the proposed ULPH model, three different particle resolutions are considered for droplet discretization, corresponding to $\Delta x = R/50$, $\Delta x = R/100$ and $\Delta x = R/200$. The maximum velocity in the domain is about $\Omega_0 R = 0.2$ m/s, and to guarantee the weakly compressible condition, the initial artificial sound speed is taken as $c_0 = 10$ m/s.

As shown in Fig. 5, the left panel illustrates the initial pressure field of the oscillating droplet with the particle resolution of $\Delta x = R/50$, the middle panel depicts the detection of particles within the free-surface region, while the right panel displays the normal vectors of particles within the same region. The results demonstrate that the proposed ULPH method can accurately calculate the normal vectors of particles within the free-surface region.

Figure 6 displays the time evolution of the shape and pressure field of the oscillating droplet during the second period with initial particle resolution $\Delta x = R/100$. Under central conservative force, the droplet first moves along the x-axis at the center point. The droplet's radius gradually decreases in the y-axis direction, while the radius in the x-axis direction increases. When the radius in the x-axis direction reaches the maximum value, the droplet reaches an equilibrium state. Under the action of the central conservative force, it starts to move along the y-axis direction from the center. When the

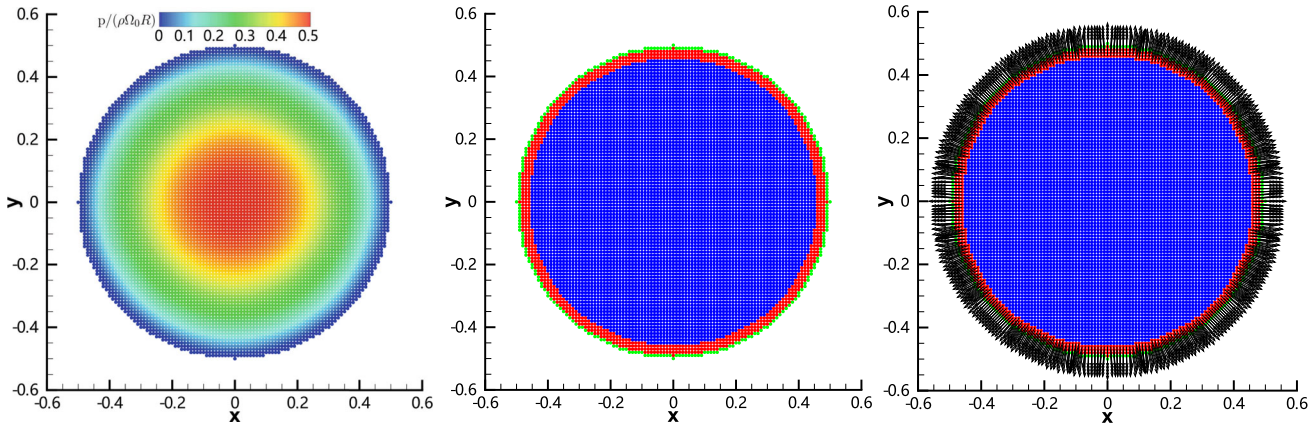

Fig. 5 Oscillating droplet subjected to a central conservative force field. Left: initial pressure field. Middle: the detection of free-surface region particles. (The free-surface particles of the droplet are marked with green color, while the free-surface vicinity particles are marked with red color. The inner particles of the droplet are colored with blue color.) Right: the normal vectors evaluated on the free-surface region. The initial particle resolution is $\Delta x = R/50$. (Color figure online)

radius reaches its maximum value in the y-axis direction, it continues to move along the x-axis, and the cycle repeats. It can be observed that the pressure field in Fig. 6 is stable and smooth when the droplet is oscillating, which shows that the density dissipation term can effectively eliminate the pressure oscillations.

The evolutions of the horizontal semi-major and vertical semi-minor axes of droplet oscillations for three particle resolutions are shown in Fig. 7, and quantitatively compared with the analytical solution [50]. It is observed that the droplet presents periodic oscillation under the action of the central conservative force. The droplet's semi-major axis in the horizontal direction and semi-minor axis in the vertical direction also present periodic changes. By comparing with the analytical solution, it can be obtained that the higher the resolution of the particles, the closer the ULPH results are to the analytical solution.

To further evaluate the accuracy and efficiency of the proposed ULPH single-phase flow model with other meshfree particle methods, we compare the time evolutions of vertical semi-minor axis of the droplet oscillations at the initial particle resolution $\Delta x = R/100$ obtained by theory, ULPH and different SPH methods, as shown in Fig. 8. It can be seen that the ULPH result and SPH result with the implementation of improved particle shifting technology (IPST) obtained by Wang et al. [48], align more closely with the analytical solution over long-term simulations. This accuracy can be attributed to the more uniform particle distribution and lower dissipation these two methods offer compared to the δ-SPH method [44]. Figure 9 further presents the comparison of execution times for first 100 timesteps of different particle resolutions, across the different methods. These simulations are all performed on a single core on the same personal computer with Intel Core i7-12700K processor. Upon increasing the number of particles, it can be found that the execution time correspondingly rose significantly. The time required by the ULPH method mirrored that of the δ-SPH method [44], while the SPH method [48] required the most time. This is because in the SPH method of Wang et al. [48], they proposed an IPST method to make the particles in the vicinity of the free surface more uniform, which is a time-consuming process. It can be concluded that the proposed ULPH method, while matching the accuracy of the SPH method [48], offers the advantage of reduced computational time.

3.2 Rotation of an initially square fluid patch

The second benchmark test case involves rotating the initially square patch of fluid, which is commonly employed to assess the stability and effectiveness of the meshfree method [48, 53, 54]. The side length of the square fluid domain is set as $L = 1$ m, as illustrated in Fig. 10. The square fluid is initialized with a rotation velocity field as

$$\begin{cases} u_0(x, y) = \hat{\omega} y \\ v_0(x, y) = -\hat{\omega} x \end{cases} \tag{44}$$

in which $\hat{\omega} = 20$ rad/s is the steady angular velocity of the square fluid. The fluid density is set to $\rho_0 = 1000$ kg/m^3. The initial pressure field [53] is obtained as

$$\begin{cases} x^* = x + \frac{L}{2} \\ y^* = y + \frac{L}{2} \\ p_0(x, y) = \rho_0 \sum_m^\infty \sum_n^\infty \frac{-32\hat{\omega}^2}{mn\pi^2[(n\pi/L)^2+(m\pi/L)^2]} \\ \quad \sin\left(\frac{m\pi x^*}{L}\right) \sin\left(\frac{n\pi y^*}{L}\right) \quad m, n \in \mathbb{N}_{odd} \end{cases} \tag{45}$$

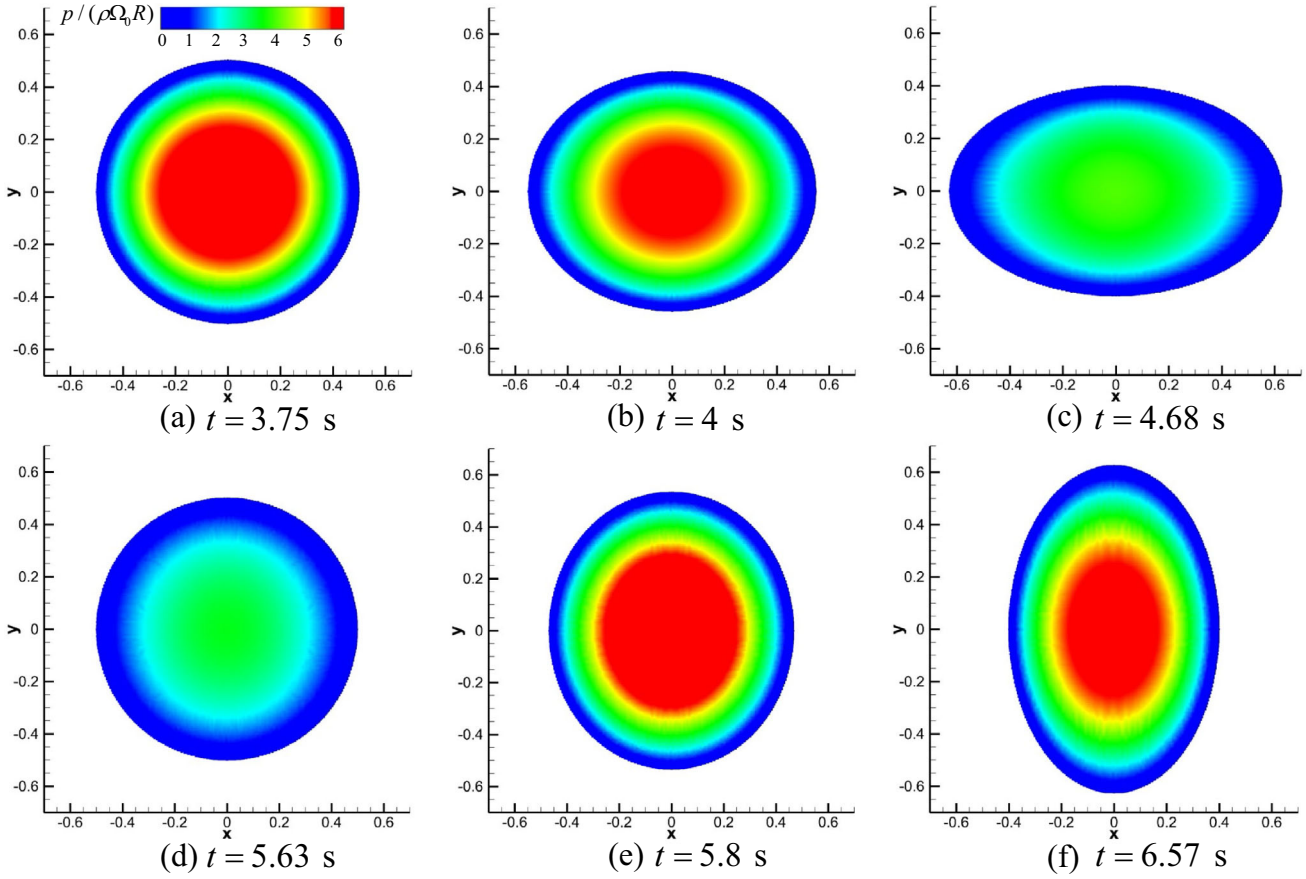

Fig. 6 The pressure field evolutions during the second period of the oscillating droplet subjected to a conservative force field

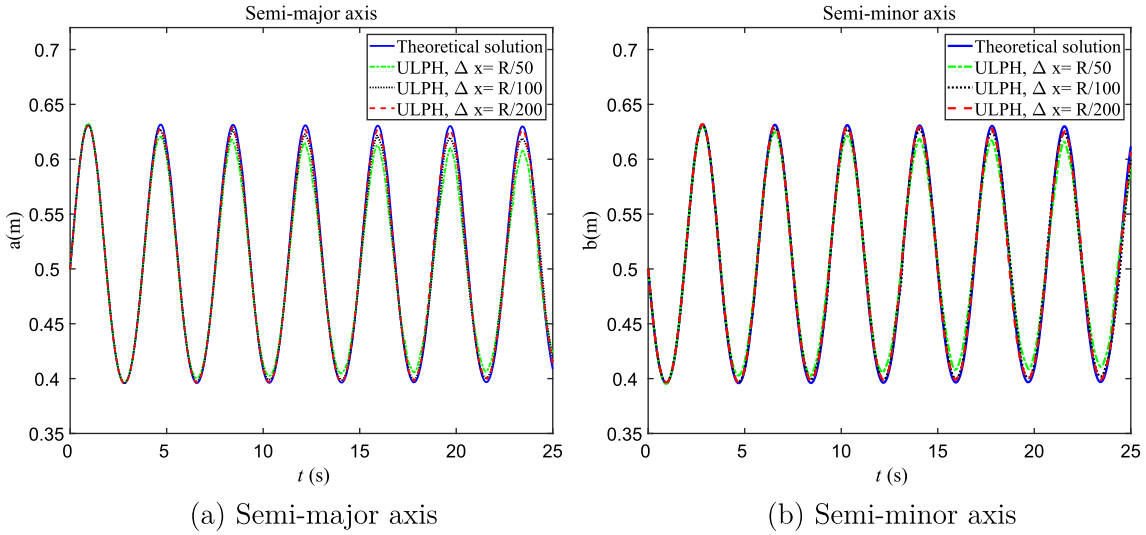

Fig. 7 The evolutions of the horizontal semi-major axis and vertical semi-minor axis of the droplet oscillations at three different particle resolutions

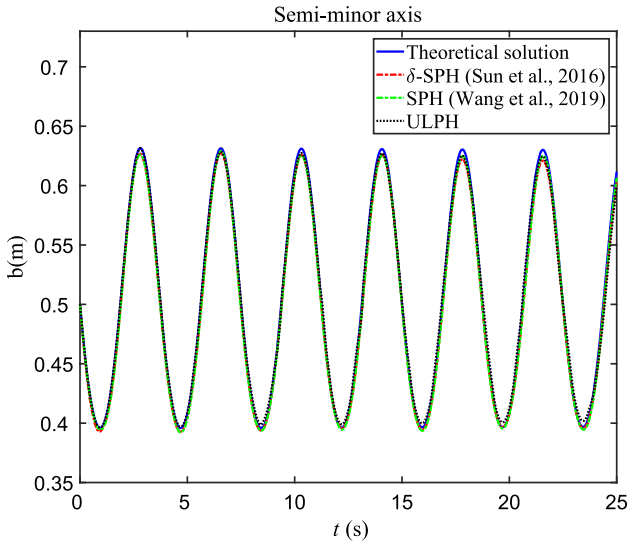

Fig. 8 Time evolutions of vertical semi-minor axis of the droplet oscillations obtained by δ-SPH, SPH and ULPH together with theoretical solution at the initial particle resolution of $\Delta x = R/100$

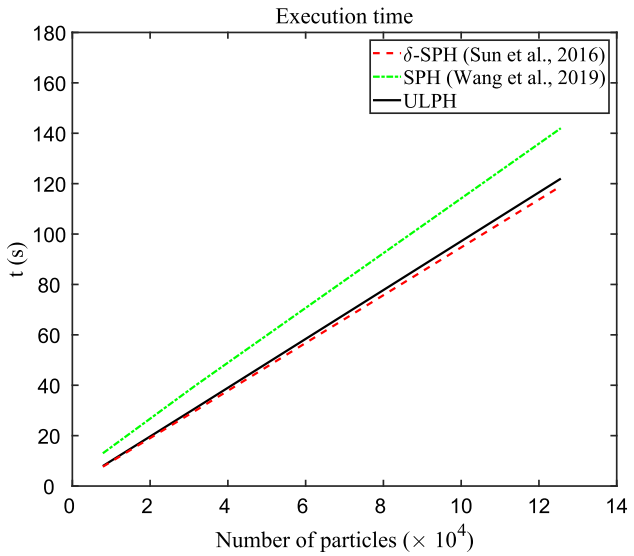

Fig. 9 Execution time comparisons for computing first 100 timesteps of the droplet oscillations calculated by different methods at different particle resolutions

The maximum expected velocity of the square fluid is $\sqrt{2}/2\hat{\omega}L$ and the initial artificial sound speed is specified as $5\sqrt{2}\hat{\omega}L$. The square fluid is discretized into initial uniform particle distributions with the particle resolutions of $\Delta x = L/100$.

Figure 11 shows the evolutions of the square fluid patch at three dimensionless times, $t\hat{\omega} = \{0.6, 1.2, 2.04\}$, and the distribution of the pressure field. The black dotted line in Fig. 11 is the free-surface result, which is computed by the Lagrangian finite difference method (FDM) [51]. Comparing the results of ULPH with those of FDM, the results of ULPH

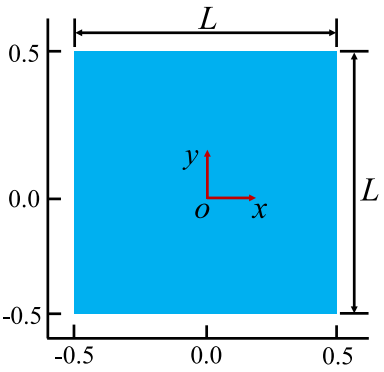

Fig. 10 Initial state of a square fluid patch

and FDM are in good agreement at the free surface, but slight differences are observed at the four sharp corners. In the rotating of the square fluid, the pressure is negative in the computational domain. However, the pressure field is still stable and smooth under negative pressure, which shows that applying PST can effectively suppress the tension instability caused by negative pressure. Figure 12 displays the velocity field of the fluid patch as the same dimensionless times in Fig. 11. It is evident that the velocity in the central area tends to 0 during the rotation, and the speed is the highest on the four spiral arms.

To obtain more shape evolution of the square fluid patch when it rotates, Fig. 13 shows the shape evolution of the fluid and the distribution of the pressure field at different dimensionless times, $t\hat{\omega} = \{4, 6, 8\}$. As time progresses, the corners of the square fluid become increasingly thin, eventually leading to fragmentation (sudden disconnection of particles at the thinnest region), which occurs due to the lack of specific resolution. When the Lagrangian finite difference method is used to simulate this example, due to the limitation of the grid, it is unable to simulate the rotational shape of the fluid after $t\hat{\omega} = 4$. Figure 14 presents the time dependent pressure curve at the center of rotating square fluid patch and compares the ULPH results with those obtained from BEM-MEL solver [51]. It can be concluded that the ULPH method has unique advantages when dealing with large deformations of free surfaces compared with the traditional grid-based methods.

3.3 Sloshing of liquid in a rectangular tank

In this subsection, liquid sloshing within a rectangular tank under horizontal excitation is numerically investigated. This liquid sloshing is a complex free-surface flow that generates nonlinear problems such as free-surface fragmentation, high-speed wall slamming, and droplet formation. Due to the complexity and nonlinear character of this phenomenon, the liquid sloshing has been studied and analyzed in several

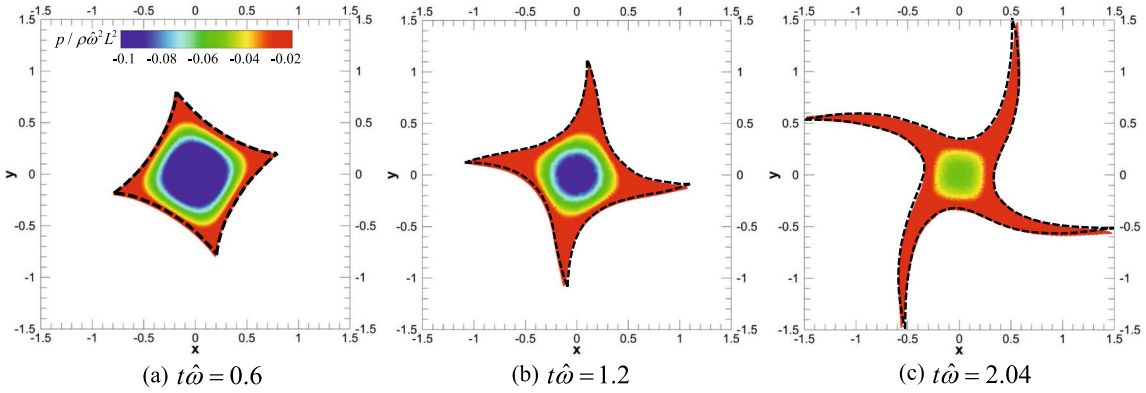

Fig. 11 Pressure fields of the rotating square fluid patch at three different dimensionless times

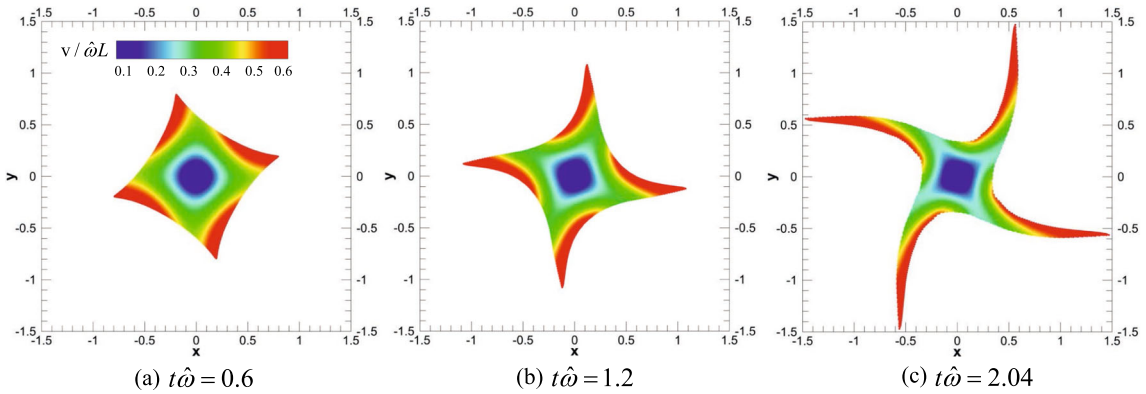

Fig. 12 Velocity fields of the rotating square fluid patch at three different dimensionless times

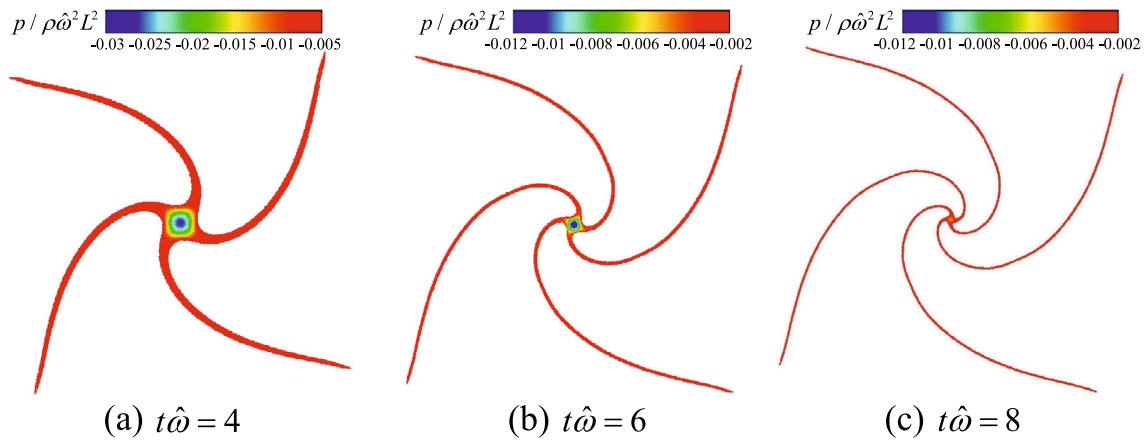

Fig. 13 Pressure fields of the rotating square fluid patch at three different time moments

academic works for model validation of meshfree method [55–58].

Figure 15 illustrates the initial setup for liquid sloshing, which corresponds to the experiment conducted by Faltinsen et al. [59]. The rectangular tank has a length of $L = 1.72$ m and a height of $H = 1.15$ m. Initially, the hight of the water in the tank is $H = 0.5$ m. To monitor the temporal evolution of the water surface height, a measuring point is positioned 0.5 m from the left wall of the rectangular tank at the free surface. The water inside the tank, which has a density of $\rho = 1000$ kg/m^3, is considered as an inviscid fluid. The acceleration of gravity is set to $g = 9.81$ m/s^2. The rectangular liquid tank is excited by a regular sinusoid in the horizontal direction (x-axis), and the velocity of the

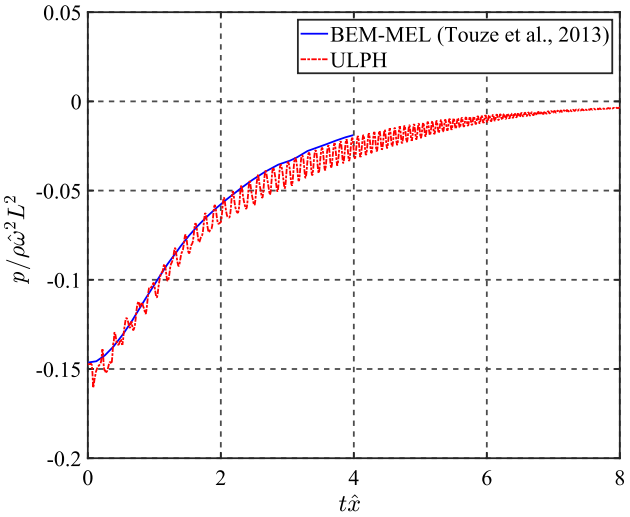

Fig. 14 The pressure time histories of the domain center of the rotating square fluid patch

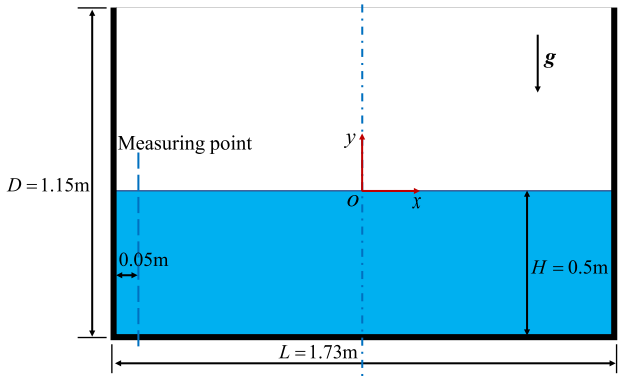

Fig. 15 Sketch of initial setup of the liquid sloshing

rectangular tank is set as

$$\begin{cases} u(t) = -\frac{2\pi}{T} A_0 \sin\left(\frac{2\pi}{T} t\right) \\ v(t) = 0 \end{cases} \tag{46}$$

in which $A_0 = 0.032$ m is the amplitude and the period is set to be $T = 1.875$ s. The initial particle distance of the computational domain is set as $\Delta x = 0.01$ m. The simulation for this example is conducted for a total of 10 s. Throughout the entire sloshing period of the liquid tank, the highest estimated velocity is 2 m/s. Furthermore, the reference sound speed is specified as $c_0 = 40$ m/s.

Figure 16 shows the evolutions of the liquid and pressure field distribution at different times of tank sloshing under horizontal excitation. As can be observed, the rectangular tank undergoes horizontal back-and-forth motion under periodic external excitation. This motion, in turn, causes the water inside the tank to move back and forth, generating significant deformation of the free surface. The pressure field of water is smooth, without pressure fluctuations, and the free-surface particle distributions are also continuous, without non-physical gaps. Therefore, it can be concluded that the ULPH single-phase flow model is stable and accurate in simulating large deformation free-surface flow problems.

Figure 17 displays the evolution of the water free-surface height at the measuring point over time and compares it with the experimental results [59]. When the rectangular tank moves cyclically along the horizontal orientation, the water surface height at the measuring point continuously increases with the sloshing period. As the time processes, the water surface height at the measuring point also becomes higher. Comparing the ULPH results with the experimental data, we can notice that the ULPH results exhibit excellent agreement with the experiment. It demonstrates that the ULPH single-phase flow model can obtain correct and stable results when simulating tank sloshing problems, and shows the expected accurate physical behavior, which lays a foundation for simulating complex three-dimensional tank sloshing problems.

3.4 Flow past a circular cylinder near a free surface

This section presents the simulation of flow past a circular cylinder placed beneath a free surface. The purpose of this investigation is to validate the significance of the proposed ULPH single-phase flow model. Similar to the previous works carried out by Reichl et al. [60] and Bouscasse et al. [61], the results of Bouscasse et al. [61] is adopted as the reference data. Figure 18 shows the initial setup of the problem. A cylinder of $d = 0.1$ m in diameter is situated in the computational domain, and its center is defined as the origin of the two-dimensional coordinate system. In the initial state, the whole fluid domain is regarded as static and the fluid density is $\rho = 1000$ kg/m^3. The distance between the undisturbed free surface and the cylinder top is defined as h_c, and the initial non-dimensional gap ratio is set to $h_c/d = 1.5$. The distance from the cylinder center to the bottom is $8d$. The inlet boundary and outlet boundary are $10d$ and $35d$ away from the cylinder center, respectively. The technique of the open boundary condition presented by Federico et al. [62] is adopted in the present work. To make the full kernel support, each wall, inlet and outlet boundary has 5 layers of particles. The bottom boundary is applied as the free-slip condition, while the cylinder is enforced with a no-slip condition.

The Froude and Reynolds numbers are used as dimensionless parameters in this study, with values of $\mathrm{Fr} = U/\sqrt{gd} = 1$ and $\mathrm{Re} = Ud/\nu = 180$, respectively. U denotes the uniform inflow velocity and ν denotes the fluid kinematic viscosity. To avoid the sudden start leading to the pressure shock wave in the flow field, the velocity of the inflow boundary increases linearly from rest to the desired velocity U with an acceleration of 1, and then the inflow velocity is kept

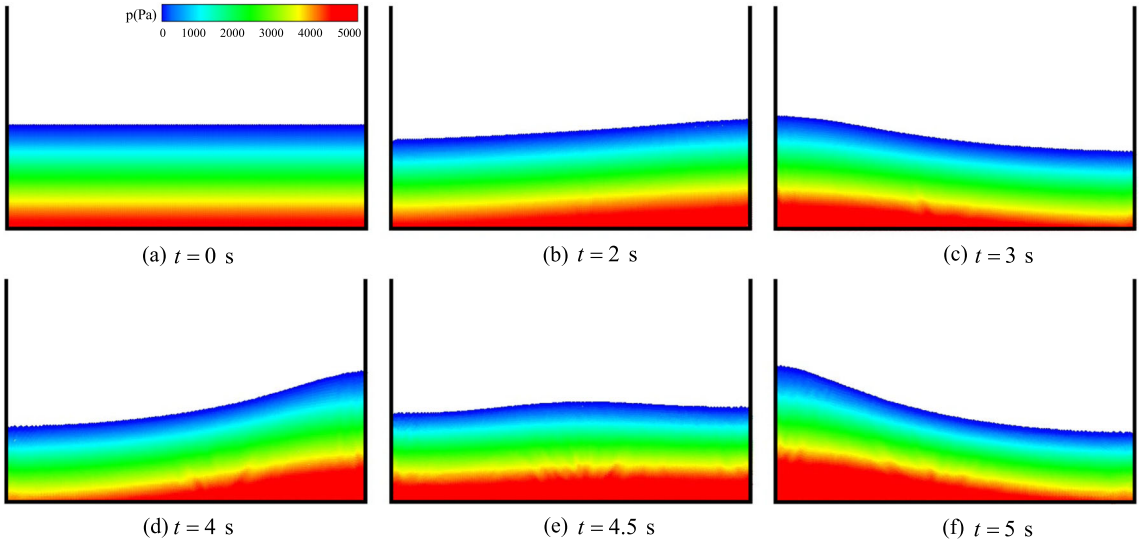

Fig. 16 The development of the free surface and pressure field distribution of the rectangular tank sloshing at different times under horizontal excitation

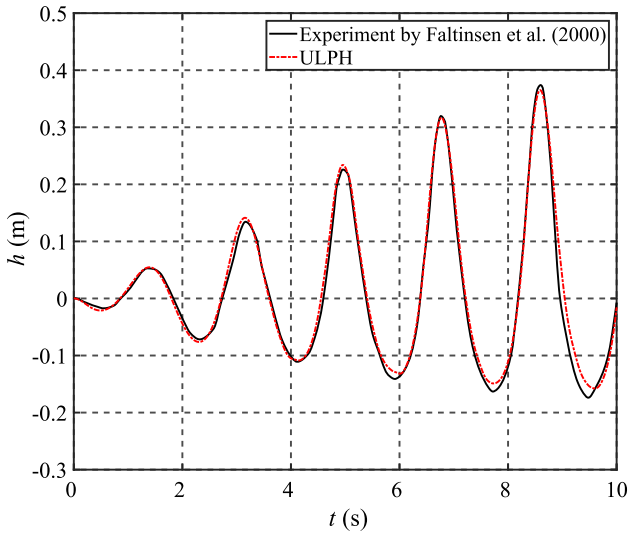

Fig. 17 Temporal evolutions of water surface height h_w at the measuring point, where red dotted line corresponds to the ULPH result, and the black solid line corresponds to the experimental result obtained by Faltinsen et al. [59]

constant. The initial particle resolution of the computational domain is set to $d/\Delta x = 25$.

Figure 19 illustrates the distributions of vorticity and free surface in the local area of the fluid field at several time instants. The von Kármán vortex shedding pattern is evident in the flow features, which is similar to the ones obtained by Bouscasse et al. [61] (see Fig. 8 in their paper). The free surface above the cylinder is lifted up by the influence of the cylinder, and forms a downward plunging jet, causing the continuous tumbling and splashing of the free surface. At the early stages of vortex shedding, the shedding vortex of the cylinder is greatly affected by the free surface and presents irregularities in the flow field, as depicted in Fig. 19b and c. Due to the periodic vortex shedding of the cylinder wake, the cyclic breaking events of the free surface take place. In the downstream region of the cylinder, the vortices generated by the free surface breaking interacts with the cylinder wave. At $t\sqrt{g/d} = 68.59$ and $t\sqrt{g/d} = 136.68$, as shown in Fig. 19d

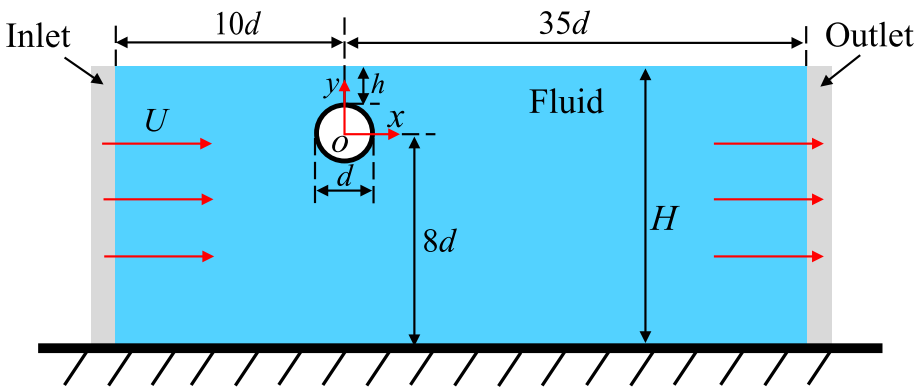

Fig. 18 Sketch of the computational domain for flow past a circular cylinder near a free surface

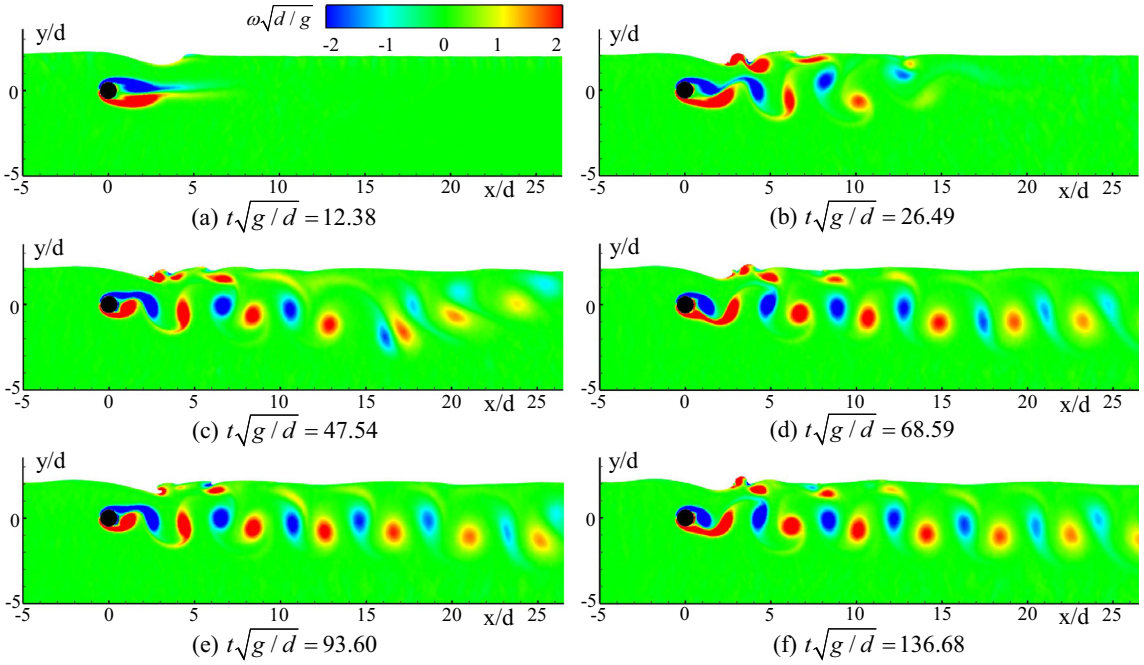

Fig. 19 Vorticity field plots of flow past a circular cylinder at different time instants

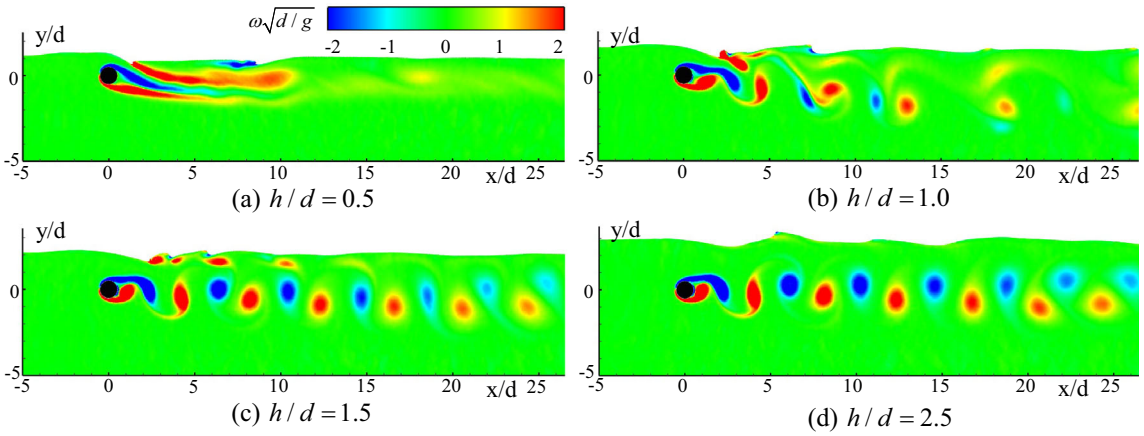

Fig. 20 Vorticity field plots for different depths at $t\sqrt{g/d}=84.19$

and f, the vorticity field of the cylinder wake is similar, but the motion characteristics of the free surface are different.

To further analyze the influence of cylinder immersion depth on flow field, different gap ratios h/d are investigated for $Fr=1$ in this part. Figure 20 depicts the vorticity field for various gap ratios ranging from $h/d=0.5$ to $h/d=2.5$ at $t\sqrt{g/d}=84.19$. The results indicate that the von Kármán vortex shedding is blocked at $h/d=0.5$, and the wake of the cylinder is nearly steady, although the free surface remains unstable. The flow jet formed downward above the cylinder interacts with the fluid behind the cylinder, resulting in the generation of a complex wake pattern downstream of the cylinder, as shown in Fig. 20a. The similar phenomena for the smaller gap ratio are demonstrated by Bouscasse et al. [61] and Colagrossi et al. [63]. As the depth of the cylinder increases, the vortex shedding phenomenon occurs at $h/d=1$. The proximity of the cylinder to the free surface results in an intense interaction between the shedding vortex and the free surface, and the wake of the cylinder cannot form periodic vortex (see Fig. 20b). The clear von Kármán vortex shedding pattern is visible, when the gap ratios h/d increase to 1.5 and 2.5, as displayed in Fig. 20c and d. The trajectory of the vortex shedding is less affected by the free surface. The cylinder wakes in Fig. 20c and d are similar, but the free surface has different motion characteristics. As can be seen from the results that the vortex shedding is clearly visible, large deformations of the free surface can be well captured, and the particles in the fluid field are uniform

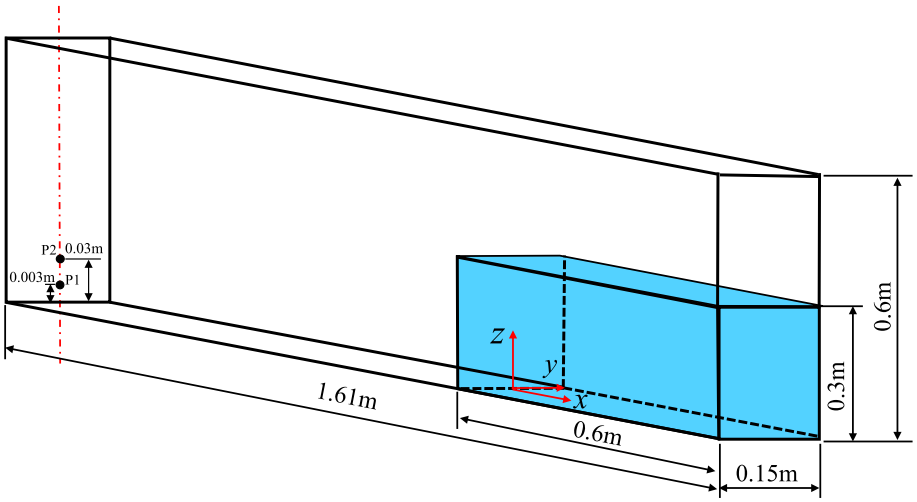

Fig. 21 Sketch of initial setup of the three-dimensional dam break

distributed without noise, which show the effectiveness and stability of the ULPH single-phase flow model.

3.5 Three-dimensional dam break

As previous test cases are all two-dimensional for validating the ULPH single-phase flow model, but in actual engineering, hydrodynamic flow exists in three-dimensional space. Hence, the ULPH single-phase flow model should be investigated for simulation enhancement of the three-dimensional case. Therefore, this section presents a simulation of a three-dimensional dam break to further validate the proposed ULPH single-phase flow model.

The initial schematic diagram of the three-dimensional dam-break is shown is Fig. 21, the initial parameters employed are based on the experimental settings of Lobovsky et al. [64]. The two pressure sensor points P1 and P2 in the Fig. 21 are located on the downstream solid wall. The length, height and width of the water column are 0.6 m, 0.3 m and 0.15 m, respectively. The water density is $\rho = 1000\ \mathrm{kg/m^3}$ and is considered as an inviscid fluid. The acceleration of gravity is $g = 9.8\ \mathrm{m/s^2}$. According to the shallow water theory, the maximum predicted velocity in the computational domain is around $v_{\max} = 2\sqrt{gH}$, in which H is water height. Therefore, the reference sound speed is determined as $c_0 = 35$ m/s. For the convenience of the simulation, the water column is released from zero initial pressure, instead of being released by quickly lifting the baffle as in the experiment. The initial particle distance of the computational domain is set as $\Delta x = 0.005$ m.

Figure 22 displays the evolution of three-dimensional dam break flow with time and the distribution of pressure field. It can be observed that after the water column is released from the initial state, it starts to flow downstream under the influence of gravity, forming a water head (see Fig. 22b and c). When the water head hits the downstream solid wall, a vertical upward jet is generated along the solid wall, as illustrated in Fig. 22d and e. It then falls downwards by gravity, forming a tongue of water (see Fig. 22f and g), falling back into the fluid below. The falling fluid impinges on the main fluid forming a secondary jet backwards and upwards. Over time, the secondary jet falls back down into the fluid by gravity, causing fragmentation and tumbling of the free surface. Throughout the numerical simulation process, the pressure field is stable and smooth, with no significant non-physical oscillations. Comparing the ULPH simulation results with the experimental data from Lobovsky et al. [64], it can be found that the ULPH results align well with the experimental results before the water head hits the downstream solid wall. After the water tongue falls back into the fluid, the ULPH results are somewhat different from the experimental results, but the overall movement trend of the fluid is consistent. The reasons for this difference can be attributed to several uncertainties such as the effect of air, turbulence, the roughness of the solid wall and the repeatability of the experiment.

Figure 23 portrays qualitative comparisons of the pressure time histories obtained by ULPH and experiment [64], which are recorded at the two pressure sensor points P1 and P2. As shown in the figure, the pressure at the measuring point P1 rises extremely after the water column hits the wall, and then gradually decreases. Due to the location of point P2 being higher than point P1, the peak pressure at point P2 is lower than point P1, but the duration of peak pressure at point P2 is longer than point P1. The comparison between the ULPH result and the experimental result shows good agreement, which further validates the accuracy and effectiveness of the ULPH single-phase flow model in simulating three-dimensional problems.

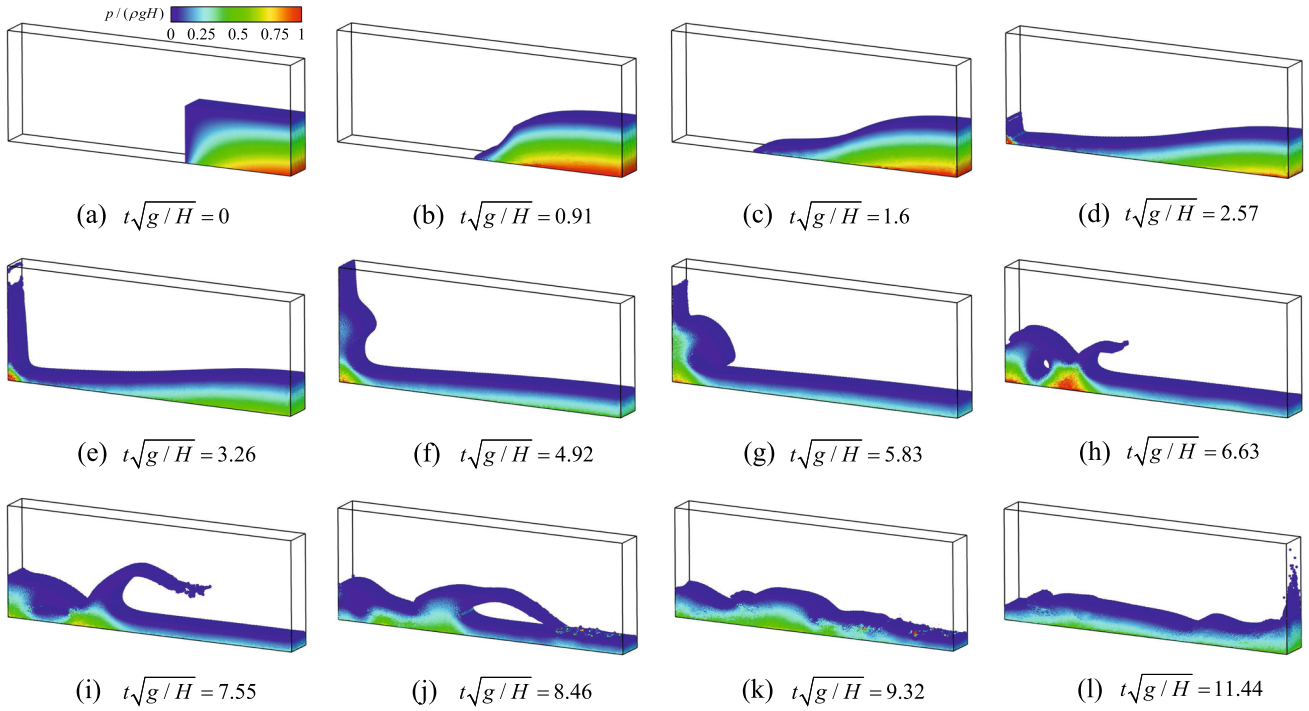

Fig. 22 The evolution and pressure field distribution of the three-dimensional dam break

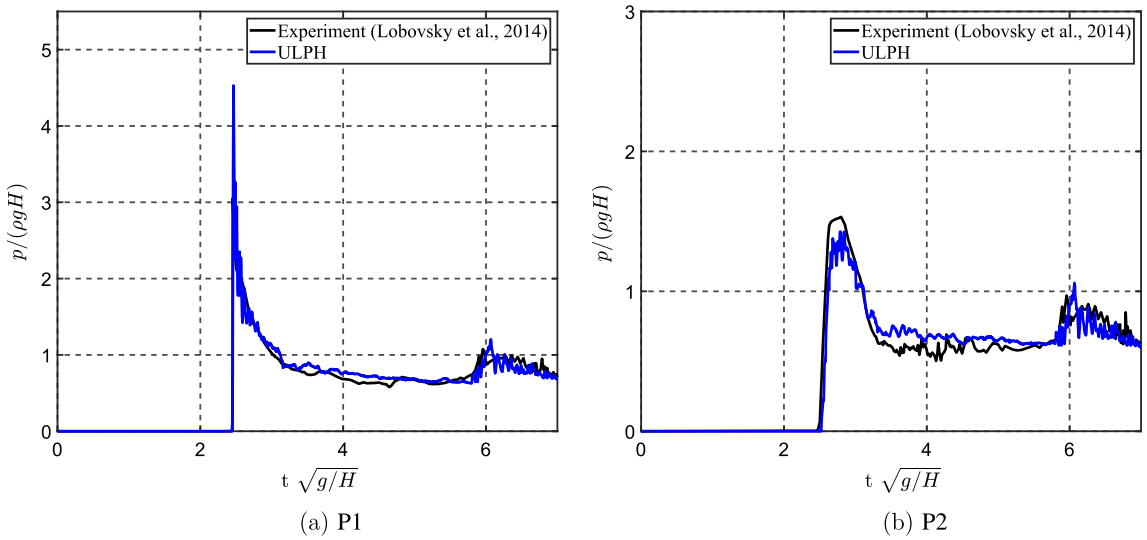

Fig. 23 The time history of pressure of ULPH results compared with experimental results [64]

4 Conclusions

In this work, we have developed a novel ULPH formulation of the single-phase surface fluid flow model for simulating complex free-surface flows. We have implemented the ULPH surface fluid flow model in numerical simulations, and further validated the proposed method. As ULPH can be regarded as a nonlocal fluid dynamics as an analog of Peridynamics in solids, the ULPH single-phase flow model established in this work further expands the application of Peridynamics in hydrodynamics. Within the ULPH framework, some enhancement techniques are proposed and integrated into the ULPH formulation to improve the accuracy and significance of numerical simulations of the ULPH method.

In specific, the conservative density diffusive term derived from the Taylor series expansion is approximated as the Laplacian of density, which is similar to the artificial viscosity term and needs some corrections according to the problem nature. The density diffusive term, when added to the continuity equation, can efficiently suppress pressure oscillation

and maintain a smooth and stable pressure field in fluid domains. The particle shifting technology is adopted for the uniform distribution of particles, and hence it helps eliminate numerical noise within the pressure/density field. The free-surface detection method demonstrates a high level of accuracy in identifying particles near the free surface and determining their normal direction in this region. In the free-surface vicinity, the shifting vectors can be adjusted based on the normal direction of the particles to improve the accuracy of the shifting magnitude. Furthermore, the optimal moment matrix is developed for the particles near the free-surface to prevent numerical instability caused by ill-conditioned matrices, which significantly improves computational efficiency.

The proposed model is tested and validated by several challenging and popular free-surface flow benchmark problems, including oscillating droplet, rotating patch, liquid sloshing, flow past circular cylinder near free surface and three-dimensional dam break. A convergence study of the oscillating droplet with different particle resolutions demonstrates that the proposed ULPH single-phase fluid flow model is convergent. Namely, the finer the resolution, the higher the accuracy that can be obtained. As shown in all conducted test examples, the ULPH single-phase flow model exhibits robust computation capabilities for complex free-surface flows, and the proposed enhancement techniques can effectively improve the accuracy and robustness of numerical simulations.

For future works, we shall carry out the sensitivity analysis on the density diffusion term in relation to energy dissipation, which needs to be studied comprehensively. It is worth utilizing the proposed model to investigate large-scale and high Reynolds number hydrodynamic problems in industrial applications. To achieve this, the efficient GPU parallel computing strategies and the Large–Eddy Simulation (LES) model in the ULPH framework will be the future directions for developments.

Acknowledgements The authors acknowledge the supports provided by the National Natural Science Foundation of China (Nos. 12293000, 12293001, 11988102, 12202011 and 12172006), China Postdoctoral Science Foundation (No. 2022M710190) and Laoshan Laboratory (No. LSKJ202200500). Moreover, we would like to thank Dr. Pingping Wang for the discussions and calculation of CPU computation times of different SPH methods. These supports are gratefully appreciated.

References

1. Moukalled F, Mangani L, Darwish M (2016) The finite volume method. In: The finite volume method in computational fluid dynamics. Springer, pp 103–135
2. Stelling G, Zijlema M (2003) An accurate and efficient finite-difference algorithm for non-hydrostatic free-surface flow with application to wave propagation. Int J Numer Methods Fluids 43(1):1–23
3. Hervouet JM (2007) Hydrodynamics of free surface flows: modelling with the finite element method. Wiley, Hoboken
4. Heyns JA, Malan AG, Harms TM, Oxtoby OF (2013) A weakly compressible free-surface flow solver for liquid–gas systems using the volume-of-fluid approach. J Comput Phys 240:145–157
5. Li Z, Ji S, Duan H, Lan S, Zhang J, Lv P (2020) Coupling effect of wall slip and spanwise oscillation on drag reduction in turbulent channel flow. Phys Rev Fluids 5(12):124601
6. Carrica P, Wilson R, Stern F (2007) An unsteady single-phase level set method for viscous free surface flows. Int J Numer Methods Fluids 53(2):229–256
7. Zhang Y, Zou Q, Greaves D (2010) Numerical simulation of free-surface flow using the level-set method with global mass correction. Int J Numer Methods Fluids 63(6):651–680
8. Monaghan JJ (1992) Smoothed particle hydrodynamics. Ann Rev Astron Astrophys 30:543–574
9. Liu M, Liu G (2010) Smoothed particle hydrodynamics (SPH): an overview and recent developments. Arch Comput Methods Eng 17(1):25–76
10. Fang X-L, Colagrossi A, Wang P-P, Zhang A-M (2022) An accurate and robust axisymmetric SPH method based on Riemann solver with applications in ocean engineering. Ocean Eng 244:110369
11. Zhang F, Zhang X, Sze KY, Lian Y, Liu Y (2017) Incompressible material point method for free surface flow. J Comput Phys 330:92–110
12. Su Y-C, Tao J, Jiang S, Chen Z, Lu J-M (2020) Study on the fully coupled thermodynamic fluid-structure interaction with the material point method. Comput Part Mech 7:225–240
13. Koshizuka S, Oka Y (1996) Moving-particle semi-implicit method for fragmentation of incompressible fluid. Nucl Sci Eng 123(3):421–434
14. Khayyer A, Gotoh H (2011) Enhancement of stability and accuracy of the moving particle semi-implicit method. J Comput Phys 230(8):3093–3118
15. Liu W, Jun S, Li S, Adee J, Belytschko T (1995) Reproducing kernel particle methods for structural dynamics. Int J Numer Methods Eng 38(10):1655–1679
16. Gingold RA, Monaghan JJ (1977) Smoothed particle hydrodynamics: theory and application to non-spherical stars. Mon Not R Astron Soc 181(3):375–389
17. Monaghan JJ (1994) Simulating free surface flows with SPH. J Comput Phys 110(2):399–406
18. He F, Zhang H, Huang C, Liu M (2022) A stable SPH model with large CFL numbers for multi-phase flows with large density ratios. J Comput Phys 453:110944
19. Marrone S, Bouscasse B, Colagrossi A, Antuono M (2012) Study of ship wave breaking patterns using 3D parallel SPH simulations. Comput Fluids 69:54–66
20. Zhang A-M, Li S-M, Cui P, Li S, Liu Y-L (2023) A unified theory for bubble dynamics. Phys Fluids 35:033323
21. Hasanpour A, Istrati D, Buckle I (2021) Coupled SPH-FEM modeling of tsunami-borne large debris flow and impact on coastal structures. J Mar Sci Eng 9(10):1068
22. Meng Z, Zhang A, Yan J, Wang P, Khayyer A (2022) A hydroelastic fluid-structure interaction solver based on the Riemann-SPH method. Comput Methods Appl Mech Eng 390:114522
23. Jandaghian M, Shakibaeinia A (2020) An enhanced weakly-compressible MPS method for free-surface flows. Comput Methods Appl Mech Eng 360:112771
24. Jandaghian M, Krimi A, Zarrati AR, Shakibaeinia A (2021) Enhanced weakly-compressible MPS method for violent free-surface flows: role of particle regularization techniques. J Comput Phys 434:110202
25. Matsunaga T, Koshizuka S (2022) Stabilized LSMPS method for complex free-surface flow simulation. Comput Methods Appl Mech Eng 389:114416

26. Sulsky D, Chen Z, Schreyer HL (1994) A particle method for history-dependent materials. Comput Methods Appl Mech Eng 118(1–2):179–196
27. Li J, Hamamoto Y, Liu Y, Zhang X (2014) Sloshing impact simulation with material point method and its experimental validations. Comput Fluids 103:86–99
28. Song Y, Liu Y, Zhang X (2020) A transport point method for complex flow problems with free surface. Comput Part Mech 7(2):377–391
29. Tu Q, Li S (2017) An updated Lagrangian particle hydrodynamics (ULPH) for Newtonian fluids. J Comput Phys 348:493–513
30. Silling SA, Epton M, Weckner O, Xu J, Askari E (2007) Peridynamic states and constitutive modeling. J Elast 88(2):151–184
31. Madenci E, Oterkus E (2013) Peridynamic theory. In: Peridynamic theory and its applications. Springer, pp 19–43
32. Lai X, Li S, Yan J, Liu L, Zhang A-M (2022) Multiphase large-eddy simulations of human cough jet development and expiratory droplet dispersion. J Fluid Mech 942:A12
33. Yan J, Li S, Kan X, Zhang A-M, Lai X (2020) Higher-order nonlocal theory of Updated Lagrangian particle hydrodynamics (ULPH) and simulations of multiphase flows. Comput Methods Appl Mech Eng 368:113176
34. Ren H, Zhuang X, Rabczuk T (2020) A higher order nonlocal operator method for solving partial differential equations. Comput Methods Appl Mech Eng 367:113132
35. Yu H, Li S (2021) On approximation theory of nonlocal differential operators. Int J Numer Methods Eng 122(23):6984–7012
36. Kan X, Yan J, Li S, Zhang A (2021) On differences and comparisons of peridynamic differential operators and nonlocal differential operators. Comput Mech 68(6):1349–1367
37. Yan J, Li S, Zhang A-M, Kan X, Sun P-N (2019) Updated Lagrangian particle hydrodynamics (ULPH) modeling and simulation of multiphase flows. J Comput Phys 393:406–437
38. Liu R, Yan J, Li S (2020) Modeling and simulation of ice-water interactions by coupling peridynamics with updated Lagrangian particle hydrodynamics. Comput Part Mech 7(2):241–255
39. Molteni D, Colagrossi A (2009) A simple procedure to improve the pressure evaluation in hydrodynamic context using the SPH. Comput Phys Commun 180(6):861–872
40. Antuono M, Colagrossi A, Marrone S, Molteni D (2010) Free-surface flows solved by means of SPH schemes with numerical diffusive terms. Comput Phys Commun 181(3):532–549
41. Marrone S, Antuono M, Colagrossi A, Colicchio G, Le Touzé D, Graziani G (2011) δ-SPH model for simulating violent impact flows. Comput Methods Appl Mech Eng 200(13–16):1526–1542
42. Xu R, Stansby P, Laurence D (2009) Accuracy and stability in incompressible SPH (ISPH) based on the projection method and a new approach. J Comput Phys 228(18):6703–6725
43. Yan J, Li S, Kan X, Zhang A-M, Liu L (2021) Updated Lagrangian particle hydrodynamics (ULPH) modeling of solid object water entry problems. Comput Mech 67(6):1685–1703
44. Sun P, Colagrossi A, Marrone S, Zhang A (2017) The δplus-SPH model: simple procedures for a further improvement of the SPH scheme. Comput Methods Appl Mech Eng 315:25–49
45. Macia Lang F, Souto Iglesias A, Antuono M, Colagrossi A (2011) Benefits of using a Wendland kernel for free-surface flows. In: 6th ERCOFTAC SPHERIC Workshop on SPH Applications
46. Sun P, Ming F, Zhang A (2015) Numerical simulation of interactions between free surface and rigid body using a robust SPH method. Ocean Eng 98:32–49
47. Zhang C, Hu X, Adams NA (2017) A weakly compressible SPH method based on a low-dissipation Riemann solver. J Comput Phys 335:605–620
48. Wang P-P, Meng Z-F, Zhang A-M, Ming F-R, Sun P-N (2019) Improved particle shifting technology and optimized free-surface detection method for free-surface flows in smoothed particle hydrodynamics. Comput Methods Appl Mech Eng 357:112580
49. Marrone S, Colagrossi A, Le Touzé D, Graziani G (2010) Fast free-surface detection and level-set function definition in SPH solvers. J Comput Phys 229(10):3652–3663
50. Monaghan JJ, Rafiee A (2013) A simple SPH algorithm for multi-fluid flow with high density ratios. Int J Numer Methods Fluids 71(5):537–561
51. Le Touzé D, Colagrossi A, Colicchio G, Greco M (2013) A critical investigation of smoothed particle hydrodynamics applied to problems with free-surfaces. Int J Numer Methods Fluids 73(7):660–691
52. Krimi A, Jandaghian M, Shakibaeinia A (2020) A WCSPH particle shifting strategy for simulating violent free surface flows. Water 12(11):3189
53. Colagrossi A (2005) A meshless Lagrangian method for free-surface and interface flows with fragmentation. These, Universita di Roma
54. Oger G, Doring M, Alessandrini B, Ferrant P (2007) An improved SPH method: towards higher order convergence. J Comput Phys 225(2):1472–1492
55. Shao J, Li H, Liu G, Liu M (2012) An improved SPH method for modeling liquid sloshing dynamics. Comput Struct 100:18–26
56. Zhang Z, Liu M (2018) A decoupled finite particle method for modeling incompressible flows with free surfaces. Appl Math Model 60:606–633
57. Rezavand M, Zhang C, Hu X (2020) A weakly compressible SPH method for violent multi-phase flows with high density ratio. J Comput Phys 402:109092
58. You Y, Khayyer A, Zheng X, Gotoh H, Ma Q (2021) Enhancement of δ-SPH for ocean engineering applications through incorporation of a background mesh scheme. Appl Ocean Res 110:102508
59. Faltinsen OM, Rognebakke OF, Lukovsky IA, Timokha AN (2000) Multidimensional modal analysis of nonlinear sloshing in a rectangular tank with finite water depth. J Fluid Mech 407:201–234
60. Reichl P, Hourigan K, Thompson MC (2005) Flow past a cylinder close to a free surface. J Fluid Mech 533:269–296
61. Bouscasse B, Colagrossi A, Marrone S, Souto-Iglesias A (2017) SPH modelling of viscous flow past a circular cylinder interacting with a free surface. Comput Fluids 146:190–212
62. Federico I, Marrone S, Colagrossi A, Aristodemo F, Antuono M (2012) Simulating 2D open-channel flows through an SPH model. Eur J Mech B/Fluids 34:35–46
63. Colagrossi A, Nikolov G, Durante D, Marrone S, Souto-Iglesias A (2019) Viscous flow past a cylinder close to a free surface: benchmarks with steady, periodic and metastable responses, solved by meshfree and mesh-based schemes. Comput Fluids 181:345–363
64. Lobovskỳ L, Botia-Vera E, Castellana F, Mas-Soler J, Souto-Iglesias A (2014) Experimental investigation of dynamic pressure loads during dam break. J Fluids Struct 48:407–434